

# Lowest-order QED radiative corrections in unpolarized elastic electron-deuteron scattering beyond the ultra-relativistic limit for the proposed deuteron charge radius measurement at Jefferson Laboratory

Jingyi Zhou<sup>a,1,2</sup>,  
Vladimir Khachatryan<sup>b,1,2,3</sup>,  
Igor Akushevich<sup>c,1</sup>,  
Haiyan Gao<sup>d,1,2</sup>,  
Alexander Ilyichev<sup>e,4,5</sup>,  
Chao Peng<sup>f,6</sup>,  
Stanislav Srednyak<sup>g,1,2</sup>,  
Weizhi Xiong<sup>h,7</sup>

<sup>1</sup>Department of Physics, Duke University, Durham, NC 27708, USA

<sup>2</sup>Triangle Universities Nuclear Laboratory, Durham, NC 27708, USA

<sup>3</sup>Department of Physics, Indiana University, Bloomington, IN 47405, USA

<sup>4</sup>Belarusian State University, Minsk, 220030, Belarus

<sup>5</sup>Institute for Nuclear Problems, Belarusian State University, Minsk, 220006, Belarus

<sup>6</sup>Physics Division, Argonne National Laboratory, Lemont, IL 60439, USA

<sup>7</sup>Key Laboratory of Particle Physics and Particle Irradiation (MOE), Shandong University, Qingdao, Shandong 266237, China

November 15, 2023

**Abstract** Analogous to the well-known proton charge radius puzzle, a similar puzzle exists for the deuteron charge radius,  $r_d$ . There are discrepancies observed in the results of  $r_d$ , measured from electron-deuteron ( $e-d$ ) scattering experiments, as well as from atomic spectroscopy. In order to help resolve the charge radius puzzle of the deuteron, the PRad collaboration at Jefferson Lab has proposed an experiment for measuring  $r_d$ , named DRad. This experiment is designed to measure the unpolarized elastic  $e-d$  scattering cross section in a low- $Q^2$  region. To extract the cross section with a high precision, having reliable knowledge of QED radiative corrections is important. In this paper, we present complete numerical calculations of the lowest-order radiative corrections in  $e-d$  scattering for the DRad kinematics. The calculations have been performed within a covariant formalism and beyond the ultra-relativistic approximation ( $m_e^2 \ll Q^2$ ). Besides, we present a systematic uncertainty on  $r_d$  arising from higher-order radiative corrections, estimated based on our cross-section results.

**Keywords** Electron-deuteron scattering, deuteron form factors, Feynman diagrams, radiative corrections, infrared divergence cancellation.

## 1 Introduction

Studies of the internal structure of the proton and neutron, as well as their simplest bound state – deuteron – help improve our understanding of quantum chromodynamics (QCD) in the nonperturbative region. The lepton scattering experiments, with the availability of precisely controlled electron beams, are well-established tools for probing the nucleon charge and magnetization distributions. In particular, if we consider the electron-proton,  $e-p$  [1–8], and electron-deuteron,  $e-d$  [9–11], scattering experiments, the conventional proton and deuteron sizes related to their internal charge distributions are given by the root-mean-square (rms) charge radii, defined as

$$r_{p|d} \equiv r_{p|d,rms} \equiv \sqrt{\langle r_{p|d}^2 \rangle} = \left( -6 \frac{dG_{E|C}^{p|d}(Q^2)}{dQ^2} \Big|_{Q^2=0} \right)^{1/2}, \quad (1)$$

where  $G_E^p$  is the proton electric form factor [12–16],  $G_C^d$  – the deuteron charge form factor [17–22], and  $Q^2$  – the four-momentum transfer squared. The proton charge radius  $r_p$  is

<sup>a</sup>jz271@duke.edu

<sup>b</sup>vladimir.khachatryan@duke.edu

<sup>c</sup>igor.akushevich@duke.edu

<sup>d</sup>haiyan.gao@duke.edu

<sup>e</sup>ily@hep.by

<sup>f</sup>cpeng@anl.gov

<sup>g</sup>stanislav.srednyak@duke.edu

<sup>h</sup>xiong@sdu.edu.cn

also extracted from the laser spectroscopy measurements of atomic hydrogen ( $eH$ ) and muonic hydrogen ( $\mu H$ ). Similarly, in addition to the scattering experiments, the deuteron charge radius  $r_d$  is determined from the spectroscopy measurements of atomic deuterium ( $eD$ ) and muonic deuterium ( $\mu D$ ).

In and after 2010, the two  $\mu H$  spectroscopy experiments reported values of  $r_p$  to be  $0.8418 \pm 0.0007$  fm [23] and  $0.8409 \pm 0.0004$  fm [24]. The world-average value from CODATA-2014 –  $r_p = 0.8751 \pm 0.0061$  fm [25] – based on the  $eH$  spectroscopy measurements, along with the results from  $e - p$  scattering experiments accomplished before 2010 mostly agree with each other, however, are larger from the  $\mu H$  results by  $\sim 7\sigma$ . This discrepancy between the  $r_p$  values, measured from those different types of experiments gave rise to the *proton charge radius puzzle* [26–28]. There are a few recent  $eH$  spectroscopy results, two of which [29, 30] are consistent with the  $\mu H$ -based  $r_p$  values within the measurement uncertainties. The PRad collaboration at Jefferson Lab [31, 32] has also reported about such an agreement with the  $\mu H$  results –  $r_p = 0.831 \pm 0.007_{\text{stat}} \pm 0.012_{\text{syst}}$  fm [7] – in an unpolarized elastic  $e - p$  scattering experiment at very low  $Q^2$  region. With all the remarkable progress until now, there are still several upcoming high-precision scattering experiments to conclusively finalize the resolution of the  $r_p$  puzzle. One of them is a new upgraded experiment at Jefferson Lab – PRad-II [33] – which will reduce the overall experimental uncertainty on  $r_p$  by a factor of  $\sim 3.8$  compared to that of PRad.

For the  $r_p$  determination in  $e - p$  scattering experiments [34, 35], we know that in addition to knowing reliably the backgrounds associated with these experiments and having tight control of systematic uncertainties, it is also necessary to carefully calculate the QED radiative corrections (RCs). Ref. [36] provides analytical formulas of a complete lowest-order RC calculations for unpolarized elastic  $e - p$  and  $e - e$  (Møller) scatterings, obtained within a covariant formalism and beyond the ultra-relativistic approximation ( $m_e^2 \ll Q^2$ ) for the kinematics of the PRad experiment<sup>1</sup>. The contribution to the total systematic uncertainty from RCs arise mostly from their higher-order contributions to the cross section [37]. If the cross-section uncertainties are turned into uncertainties on  $r_p$ , then the absolute RC systematic uncertainty in PRad for  $e - p$  due to higher-order RCs is 0.0020 fm, whereas it is 0.0065 fm for the Møller process [7]. The total RC systematic uncertainty is  $\Delta r_p = 0.0069$  fm.

Interestingly enough, there is also the *deuteron charge radius puzzle* in determination of  $r_d$  in  $e - d$  scattering experiments and  $eD/\mu D$  spectroscopy measurements. Since 1998, the  $r_d$  input (determined from elastic  $e - d$  scattering data) in the CODATA adjustment is  $r_d = 2.13 \pm 0.01$  fm,

<sup>1</sup>In the PRad experiment, most of the systematic uncertainties are correlated and  $Q^2$ -dependent

obtained in [38, 39]. Meanwhile, the most recent scattering-based  $r_d$  input in the CODATA-2018 adjustment [40] is  $r_d = 2.111 \pm 0.019$  fm. In 2016, the CREMA collaboration has reported a deuteron charge radius value –  $r_d = 2.12562 \pm 0.00078$  fm – from a  $\mu D$ -based spectroscopy measurement of three  $2P \rightarrow 2S$  transitions in  $\mu D$  atoms [41], which is  $3.2\sigma$  smaller than the CODATA-2018 world-average value:  $r_d = 2.12799 \pm 0.00074$  fm [40]. On the other hand, the radius from [41] is  $3.5\sigma$  smaller than  $r_d = 2.1415 \pm 0.0045$  fm determined from an  $eD$ -based measurement [42] of  $1S \rightarrow 2S$  transitions in  $eD$  atoms, along with these transitions measured in [43].

The uncertainties from all previous  $e - d$  scattering experiments are too large to contribute to a satisfactory resolution of the  $r_d$  puzzle. In this respect, the PRad collaboration has proposed a new high-precision magnetic-spectrometer-free, calorimeter-based unpolarized elastic  $e - d$  scattering experiment (named DRad [44]) at the scattering angle range  $\theta_e = 0.7^\circ - 6.0^\circ$ , and at electron beam energies  $E_1 = 1.1$  GeV and 2.2 GeV, which corresponds to  $Q^2 = 2 \times 10^{-4} (\text{GeV}/c)^2 - 5 \times 10^{-2} (\text{GeV}/c)^2$ . The DRad experiment is designed to utilize the PRad-II experimental setup, by adding a low-energy cylindrical recoil detector for ensuring the elasticity of the  $e - d$  scattering process. The proposed experiment will allow a model-independent extraction of  $r_d$  with a precision  $\sim 0.2\%$  for addressing the  $r_d$  puzzle. One should note that the Møller scattering will be simultaneously measured in the DRad experiment, making use of the same procedure and tools that have been deployed in PRad, for controlling the systematic uncertainties associated with the absolute  $e - p$  and  $e - d$  cross-section measurements along with monitoring the luminosity. Moreover, it is similarly necessary to carefully calculate the QED RCs for this experiment. For this purpose, we will use the RC covariant framework developed in [36, 45–53] to perform calculations on the lowest-order Feynman diagrams for unpolarized elastic  $e - d$  scattering<sup>2</sup>. In our final results the electron mass  $m_e$  is taken into account. In this framework, the Bardin-Shumeiko approach is used for the covariant extraction and cancellation of infrared divergences [70, 71]. At this point, we wish to emphasize that the differential cross section of elastic scattering of deuterons on electrons at rest has been studied theoretically with great details taking model-independent QED RCs into account [72], in which a high-energy incident deuteron and a recoil electron are both considered to be detected in a coincidence experimental setup, resulting in kinematic coverages at very low  $Q^2$ .

It is also relevant to indicate some recent phenomenological and theoretical developments related to the deuteron radius extraction. Like Ref. [73], in which a robust extraction

<sup>2</sup>For alternative lowest- and also higher-order RC calculations and event generators, we refer to Refs. [54–61] in unpolarized lepton-proton scattering and to Refs. [59, 62–69] in lepton-lepton scattering.

of  $r_d$  prior to the DRad data taking is carried out, based on the “root mean square error (RMSE)” method developed by the PRad collaboration in [74]. Ref. [75] shows an alternative robust extraction of  $r_d$  using the “statistical Schlessinger point method (SPM)” first applied to the  $r_p$  extraction by Craig Roberts and his collaborators in [76]. Refs. [77, 78] present high-accuracy calculations of the deuteron radius in chiral effective field theory, along with the determination of the neutron charge radius, by Evgeny Epelbaum and his collaborators.

Our paper is organized as follows. In Sec. 2, we discuss the unpolarized elastic  $e - d$  differential cross section. A short overview of the deuteron four data-based electromagnetic form-factor models (with pertinent details) is given in Appendix A because the final cross sections include the form-factor parametrizations of the deuteron. In Sec. 3, we first discuss the kinematics of the process, and then discuss in detail the model-independent lowest-order RCs in  $e - d$ , including corrections stemming from a lepton vertex function, vacuum polarization, and radiation of a real photon from leptonic legs. Sec. 4 presents numerical results on the computed final cross sections, and estimation of the lowest-order RC systematic uncertainty on  $r_d$  for the DRad experiment. We summarize and provide prospects in the last section.

## 2 Electron-deuteron unpolarized elastic cross section and deuteron electromagnetic form-factor models

One of the fundamental problems in modern nuclear physics is to understand the deuteron’s electromagnetic structure, given that it is the only naturally-existing two-nucleon bound system. Elastic scattering in the  $e - d$  process is more complicated than that in the  $e - p$  process, however, it is anticipated that at low  $Q^2$  the deuteron form factors are controlled by part of its wave function, for which the two nucleons are quite apart. This is because the non-nucleonic degrees of freedom and relativistic effects inside the deuteron are expected to be insignificant. As a consequence, theoretical computations of the deuteron form factors and rms radius are considered to be well grounded since those are independent of a broad class of nucleon-nucleon potentials, and depend mostly on the neutron-proton scattering length and their binding energy [79]. This makes, e.g.,  $r_d$  an ideal observable for theory-experiment comparisons.

In the general case of the  $e - d$  scattering process, the four-momentum and helicity of incident & scattered electrons off a spin-1 deuteron fixed target are  $(k_1, \sigma_1)$  &  $(k_2, \sigma_2)$ , respectively, and the corresponding quantities for the target are  $(p_1, \lambda_1)$  &  $(p_2, \lambda_2)$  (see Fig. 1).

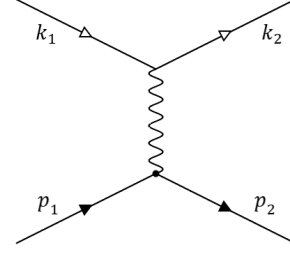


**Fig. 1** Feynman diagram contributing to the Born cross section for the elastic  $e - d$  scattering. Only the four-momenta of the electron and deuteron are shown.

The matrix element of the electromagnetic current operator for this process has the following form [19, 80]:

$$\mathcal{M} = ie^2 \bar{u}(k_2, \sigma_2) \gamma^\mu u(k_1, \sigma_1) \frac{1}{q^2} \langle p_2, \lambda_2 | j_\mu | p_1, \lambda_1 \rangle, \quad (2)$$

where  $\bar{u}$  and  $u$  are the Dirac spinors,  $q^2 = (p_2 - p_1)^2 = (k_1 - k_2)^2$  is the four-momentum transfer squared carried by the exchanged virtual photon. The electromagnetic current operator for the deuteron is given by

$$\begin{aligned} \langle p_2, \lambda_2 | j_\mu | p_1, \lambda_1 \rangle &\equiv G_{\lambda_2, \lambda_1}^\mu(p_2, p_1) = \\ &= - \left\{ G_1^d(q^2) (\xi_{\lambda_2}^*(p_2) \cdot \xi_{\lambda_1}(p_1)) (p_2 + p_1)^\mu + \right. \\ &\quad + G_2^d(q^2) \left[ \xi_{\lambda_1}^\mu(p_1) (\xi_{\lambda_2}^*(p_2) \cdot q) - \right. \\ &\quad \quad \left. \left. - \xi_{\lambda_2}^{\mu*}(p_2) (\xi_{\lambda_1}(p_1) \cdot q) \right] - \right. \\ &\quad \left. - G_3^d(q^2) \frac{1}{2M_d^2} (\xi_{\lambda_2}^*(p_2) \cdot q) (\xi_{\lambda_1}(p_1) \cdot q) \times \right. \\ &\quad \quad \left. \times (p_2 + p_1)^\mu \right\}, \quad (3) \end{aligned}$$

where  $M_d$  is the deuteron mass ( $= 1875.612$  MeV).  $\xi_1 \equiv \xi_{\lambda_1}^\mu(p_1)$  and  $\xi_2 \equiv \xi_{\lambda_2}^{\mu*}(p_2)$  are the polarization four-vectors of the initial and final deuteron states, satisfying the condition of  $\xi_1 \cdot p_1 = \xi_2 \cdot p_2$ .

For electron scattering, since the virtual photon four-momentum is always space-like, the convention  $Q^2 \equiv -q^2$  is adopted. The  $Q^2$ -dependent form factors  $G_i^d$  in Eq. (3) are related to the charge monopole ( $G_C^d$ ), magnetic dipole ( $G_M^d$ ), and charge quadrupole ( $G_Q^d$ ) form factors via

$$\begin{aligned} G_C^d(Q^2) &= G_1^d(Q^2) + \frac{2}{3} \eta G_Q^d(Q^2), \\ G_M^d(Q^2) &= G_2^d(Q^2), \\ G_Q^d(Q^2) &= G_1^d(Q^2) - G_2^d(Q^2) + (1 + \eta) G_3^d(Q^2), \quad (4) \end{aligned}$$

with  $\eta = Q^2 / (4M_d^2)$ . Besides, there are the following additional relations that are normalized such that

$$G_C^d(0) = 1, \quad \frac{G_M^d(0)}{\mu_M^d} = 1, \quad \frac{G_Q^d(0)}{\mu_Q^d} = 1, \quad (5)$$

with the given deuteron magnetic dipole moment ( $\mu_M^d$ ) and electric quadrupole moment ( $\mu_Q^d$ )<sup>3</sup>.

The cross section for elastic scattering of longitudinally polarized electrons off a polarized deuteron target is calculated in the rest frame of the deuteron, within the Born approximation assuming one-photon exchange [19, 80, 81]. Nonetheless, the electron beam and the deuteron target in the DRad experiment are planned to be unpolarized. Therefore, we are interested in the process of

$$e(k_1) + d(p_1) \rightarrow e'(k_2) + d(p_2), \quad (6)$$

and in using the following well-known Born cross section of the unpolarized elastic  $e-d$  scattering at low  $Q^2$  [9–11, 80, 82–84]:

$$\frac{d\sigma^B}{d\theta_e}(E_1, \theta_e) = \sigma_{NS}(E_1, \theta_e) \times \left( A_d(Q^2) + B_d(Q^2) \tan^2\left(\frac{\theta_e}{2}\right) \right). \quad (7)$$

Here the unpolarized elastic structure functions  $A_d(Q^2)$  and  $B_d(Q^2)$  are defined as

$$\begin{aligned} A_d(Q^2) &= (G_C^d(Q^2))^2 + \frac{2}{3} \eta (G_M^d(Q^2))^2 + \\ &\quad + \frac{8}{9} \eta^2 (G_Q^d(Q^2))^2, \\ B_d(Q^2) &= \frac{4}{3} \eta(1 + \eta) (G_M^d(Q^2))^2, \end{aligned} \quad (8)$$

and  $\sigma_{NS}$  is the differential Mott cross section for the elastic scattering from a point-like and spinless particle at the electron scattering angle  $\theta_e$  and the incident energy  $E_1$  [85]:

$$\begin{aligned} \sigma_{NS}(E_1, \theta_e) &\equiv \left( \frac{d\sigma}{d\theta_e}(E_1, \theta_e) \right)_{\text{Mott}} = \\ &= 2\pi \frac{4\alpha^2 E_2^2 E_1}{Q^4} \left( 1 - \sin^2\left(\frac{\theta_e}{2}\right) \right) \sin(\theta_e). \end{aligned} \quad (9)$$

where  $\alpha = e^2/4\pi = 1/137.036$  is the electromagnetic fine-structure constant. It should be mentioned that in the literature the cross sections in Eq. (7) and Eq. (9) are usually given as  $d\sigma/d\Omega$ . Meanwhile, we use the relation  $d\Omega = \sin(\theta_e) d\theta_e d\varphi$ , and uniformly integrate the cross section over the azimuthal angle  $\varphi$  from 0 to  $2\pi$  limits<sup>4</sup>.

Generally, if we consider the lepton-deuteron scattering, its energy conservation reads as [86]

$$M_d(E_1 - E_2) = E_1 E_2 - |\mathbf{p}_1| |\mathbf{p}_2| \cos(\theta_l) - m_l^2. \quad (10)$$

The scattered lepton energy  $E_2$  is solved to be

$$E_2 = \frac{B + \sqrt{B^2 + 4AC}}{-2A}, \quad (11)$$

<sup>3</sup>Throughout our work, we use dimensionless quantities  $G_M^d(0) = 1.714$ ,  $\mu_M^d \equiv (\mu_M^d/\mu_N) = 0.8574$ , and  $G_Q^d(0) = 25.830$ ,  $\mu_Q^d \equiv (\mu_Q^d/\text{fm}^2) = 0.2859$  [19].

<sup>4</sup>In Appendix B, we show  $Q^2$ -dependent Born cross section (equivalent to Eq. (7)) derived in the ansatz of [36, 52].

where

$$\begin{aligned} A &= (E_1^2 - m_l^2) \cos^2(\theta_l) - E_1^2 - 2M_d E_1 - M_d^2, \\ B &= 2(m_l^2 + M_d^2) E_1 + 2M_d(m_l^2 + E_1^2), \\ C &= (m_l^2 E_1^2 - m_l^4) \cos^2(\theta_l) + \\ &\quad + m_l^4 + 2m_l^2 M_d E_1 + M_d^2 E_1^2. \end{aligned} \quad (12)$$

In the limit of  $E_1/m_l$ ,  $E_2/m_l$ ,  $M_d/m_l \gg 1$  (which is the case for the  $e-d$  scattering in the DRad kinematics), Eq. (11) reduces to

$$E_2 = \frac{E_1}{1 + (2E_1/M_d) \sin^2(\theta_l/2)}. \quad (13)$$

Another relation between the momentum transfer squared and the scattering angle is

$$q^2 = 2(m_l^2 - E_1 E_2 + |\mathbf{p}_1| |\mathbf{p}_2| \cos(\theta_l)), \quad (14)$$

which brings to

$$\cos(\theta_l) = \frac{2E_1 E_2 - 2m_l^2 - Q^2}{2\sqrt{E_1^2 - m_l^2} \sqrt{E_2^2 - m_l^2}}, \quad (15)$$

If one neglects the lepton mass, it reduces to another well-known formula of  $Q^2 = 4E_1 E_2 \sin^2(\theta_l/2)$ , however, as it is mentioned in the introduction, the DRad experiment will reach low  $Q^2 \sim 10^{-4} (\text{GeV}/c)^2$  region, where it is necessary to keep  $m_l$  in Eq. (15). The lowest-order RC results and the total (observed) cross section are in particular obtained in Sec. 3, with  $m_l$  taken in calculations into account that is beyond the ultra-relativistic approximation.

On the other hand, Eq. (7) has been derived in literature by neglecting the electron (lepton) mass, however, its inclusion into that formula would not affect the cross section determination with very high accuracy, at JLab and Mainz beam energies. The reason is that in the extraction of  $r_p$  [7, 87], based on using a similar Born cross-section formula for unpolarized elastic  $e-p$  scattering at low  $Q^2$ , there were essentially no changes in the  $r_p$  central value and its total systematic uncertainty, with and without the electron mass included in the Born cross section. Furthermore, the massless Born formula in Eq. (7) has been used by the Mainz Microtron A1 collaboration for the deuteron form-factor precise measurements in the elastic  $e-d$  scattering [20, 21].

### 3 Lowest-order QED radiative corrections to the unpolarized elastic $e-d$ scattering cross section

In this section, we deploy some of the key formulas and derivations from Refs. [36, 52] (partially used in the ansatz of [45, 48, 88] too) since those expressions can also be used for the unpolarized elastic  $e-d$  scattering, as far as the DRad experiment is concerned. Meanwhile, one should mention that all the RC and cross-section formulas represented here

are obtained within the covariant Bardin-Shumeiko formalism [70, 71], which is applied to the extraction and cancellation of infrared divergences stemming from virtual and real photon radiation in the scattering process under consideration. The ultimate results derived within this formalism are independent of any unphysical and artificial parameters, like the cut-off parameter existing in the Mo-Tsai approach [89, 90], introduced for separation of the regions of soft and hard photon radiation, while canceling out the infrared divergences in the pertinent Feynman diagram calculations.

### 3.1 Kinematics of the Bremsstrahlung process

The Feynman diagram of the Born process is already shown in Fig. 1. The other diagrams of interest for computations of the lowest-order RCs are demonstrated in Fig. 2, which show the vertex correction (a), the vacuum polarization (b), as well as the bremsstrahlung (c) and (d) originating from the leptonic legs. Let us start by considering the process

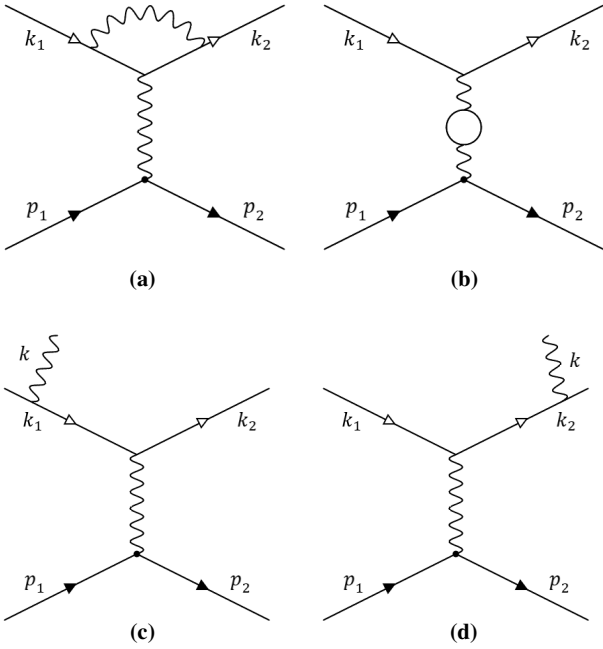


**Fig. 2** Feynman diagrams from (a) to (d), describing the lowest-order QED RC contributions to the unpolarized elastic  $e - d$  scattering cross section: (a) vertex correction; (b) vacuum polarization; (c), (d) electron-leg bremsstrahlung.

of bremsstrahlung with a radiated hard photon,  $\gamma(k)$ , represented as

$$e(k_1) + d(p_1) \rightarrow e'(k_2) + d(p_2) + \gamma(k), \quad (16)$$

the cross section of which is given by

$$d\sigma_R = \frac{1}{2\sqrt{\lambda_S}} \mathcal{M}_R^2 d\Gamma_3, \quad (17)$$

where

$$\lambda_S = S^2 - 4m_e^2 M_d^2, \quad \text{with } S = 2k_1 \cdot p_1 = 2E_1 \cdot M_d. \quad (18)$$

For the matrix element squared  $\mathcal{M}_R^2$ , we refer to the equation (49) in [52], and the equation (14) in [36]. The phase-space element  $d\Gamma_3$  can be described in terms of three additional quantities (“photonic variables”). For such an expression of the phase space, we refer to equation (48) in [52]. We choose the standard set of photonic variables to be

$$v = (p_1 + k_1 - k_2)^2 - M_d^2, \quad \tau = \frac{k \cdot q}{k \cdot p_1}, \quad \phi_k, \quad (19)$$

in which  $v$  is the inelasticity, and  $\phi_k$  is the azimuthal angle between  $(\mathbf{k}_1, \mathbf{k}_2)$  and  $(\mathbf{k}, \mathbf{q})$  planes in the rest frame ( $\mathbf{p}_1 = 0$ ). The upper limit for  $v$  at fixed  $Q^2$  is

$$v_q = \frac{\sqrt{\lambda_S} \sqrt{\lambda_m} - Q^2 (S + 2m_e^2)}{2m_e^2}. \quad (20)$$

where the function  $\lambda_m$  is given by

$$\lambda_m = Q^2 (Q^2 + 4m_e^2), \quad (21)$$

When  $Q^2$  is near its kinematic boundaries, the maximum value of the inelasticity  $v_q$  is determined to be

$$v_q^{\max} = S - 2m_e \left( \sqrt{S + m_e^2 + M_d^2} - m_e \right). \quad (22)$$

In practice, the real hard photon contribution to the observed cross section can be considerably reduced by applying a cut on the inelasticity quantity. This cut in turn is a measured quantity in single-arm measurements of elastically scattered leptons only. Keeping in mind the maximum value  $v_q^{\max}$ , throughout this section we use an experimentally observable variable,  $v_{\text{cut}}$ , for the upper limit of the inelasticity (both for the fixed  $Q^2$  and  $\theta_e$ ). Sec. 4.1 discusses more details on  $v_{\text{cut}}$ .

### 3.2 Lowest-order radiative corrections and the observed cross section

We use Eqs. (7), (8), (9), and (13) for the unpolarized elastic  $e - d$  Born cross section in our current analysis. The equivalent cross section is also shown in Appendix B. The  $Q^2 \leftrightarrow \theta_e$  transformation is given by Eq. (15), otherwise expressed as

$$Q^2 = 2E_1 E_2 - 2m_e^2 - 2\sqrt{E_1^2 - m_e^2} \sqrt{E_2^2 - m_e^2} \cos(\theta_e), \quad (23)$$

On the other hand, from Ref. [52] we have

$$\frac{d\sigma^B}{dQ^2} = -\frac{1}{j_\theta \sin(\theta_e)} \frac{d\sigma^B}{d\theta_e}, \quad (24)$$

or just

$$dQ^2 = -j_\theta \sin(\theta_e) d\theta_e, \quad (25)$$

where the transformation Jacobian is represented by

$$j_\theta = -\frac{\sqrt{\lambda_S} \lambda_X^{3/2}}{2M_d^2 (SX - 2m_e^2 (Q^2 + 2M_d^2))}, \quad (26)$$

and where  $\lambda_X$  and  $X$  are shown below in Eq. (34) and Eq. (36), respectively. Eq. (25) is equivalent to the following relation derived from Eq. (23):

$$dQ^2 = -\left[ \frac{2}{M_d} E_1 E_2^2 - \frac{2}{M_d} \frac{\sqrt{E_1^2 - m_e^2} E_2^3}{\sqrt{E_2^2 - m_e^2}} \cos(\theta_e) - 2\sqrt{E_1^2 - m_e^2} \sqrt{E_2^2 - m_e^2} \sin(\theta_e) \right] d\theta_e. \quad (27)$$

The observed cross section as functions of  $Q^2$  and  $\theta_e$  for the unpolarized elastic  $e - d$  scattering beyond ultra-relativistic approximation, including the lowest-order RC contributions, is expressed as follows:

$$\begin{aligned} \frac{d\sigma^{\text{obs}}}{dQ^2} = & \left[ 1 + \right. \\ & \left. + \frac{\alpha}{\pi} \left( \delta_{VR}(Q^2) + \delta_{\text{vac}}^l(Q^2) + \delta_{\text{vac}}^h(Q^2) - \delta_{\text{inf}}(Q^2) \right) \right] \times \\ & \times \left[ e^{(\alpha/\pi) \delta_{\text{inf}}(Q^2)} \right] \frac{d\sigma^B}{dQ^2} + \frac{d\sigma^{\text{AMM}}}{dQ^2} + \frac{d\sigma_R^F}{dQ^2}, \quad (28) \end{aligned}$$

$$\begin{aligned} \frac{d\sigma^{\text{obs}}}{d\theta_e} = & \left[ 1 + \right. \\ & \left. + \frac{\alpha}{\pi} \left( \delta_{VR}(\theta_e) + \delta_{\text{vac}}^l(\theta_e) + \delta_{\text{vac}}^h(\theta_e) - \delta_{\text{inf}}(\theta_e) \right) \right] \times \\ & \times \left[ e^{(\alpha/\pi) \delta_{\text{inf}}(\theta_e)} \right] \frac{d\sigma^B}{d\theta_e} + \frac{d\sigma^{\text{AMM}}}{d\theta_e} + \frac{d\sigma_R^F}{d\theta_e}, \quad (29) \end{aligned}$$

Let us now describe in details and discuss all the terms in Eq. (28) and Eq. (29).

- **RC term  $\delta_{VR}$ .** In order to extract the infrared divergences correctly, one should use the following transformation:

$$d\sigma_R = (d\sigma_R - d\sigma_R^{IR}) + d\sigma_R^{IR} = d\sigma_R^F + d\sigma_R^{IR}, \quad (30)$$

where  $\sigma_R^F$  and  $\sigma_R^{IR}$  on the r.h.s. are the infrared divergence-free and divergence-dependent contributions of the cross section, respectively.  $\sigma_R^F$  becomes finite when  $k \rightarrow 0$ .  $\sigma_R^{IR}$  can be obtained before integration over the variable  $\phi_k$ , as a factorized term in front of the Born cross section:

$$\frac{d\sigma_R^{IR}}{dQ^2} = \frac{1}{R} \lim_{R \rightarrow 0} \left[ R \frac{d\sigma_R}{dQ^2} \right] = -\frac{\alpha}{\pi^2} \frac{F_{IR}}{R^2} \frac{d^3k}{k_0} \frac{d\sigma^B}{dQ^2}, \quad (31)$$

where the variable  $R$  reads as

$$R = 2k \cdot p_1 = \frac{v}{1 + \tau}, \quad (32)$$

and for the function  $F_{IR}$ , one should refer to the equations (54), (59) and (60) in [52].

Afterwards,  $d\sigma_R^{IR}/dQ^2$  needs to be separated into a soft  $\delta_S$  and a hard  $\delta_H$  parts by splitting the integration region over the inelasticity  $v$ , which can be done by introducing an infinitesimal photon energy  $\lambda \rightarrow 0$  that is defined in the system  $\mathbf{p}_1 + \mathbf{q} = 0$ . For the formulas of  $\delta_S$  and  $\delta_H$ , we refer to the equation (62) in [52]. For the infrared sum  $\delta_{IR} = \delta_S + \delta_H$ , we quote the equation (63) in [52] and the equation (26) in [36].

In order to cancel the infrared divergences, one should also consider the leptonic vertex correction,  $\delta_{\text{vert}}$ , in the panel (a) of Fig. 2.  $\delta_{\text{vert}}$  is shown by the equation (41) in [52], the equation (36) in [36], the equation (20) in [45], and the equation (50) in [48]. Ultimately, the sum of all infrared divergent terms that is now  $\delta_{IR} + \delta_{\text{vert}}$  results in an expression, which is itself free from any infrared divergence. Notably, the components containing the infinitesimal photon energy  $\lambda$  cancel out explicitly in what is represented as follows:

$$\begin{aligned} \delta_{VR}(Q^2) = & \delta_{IR} + \delta_{\text{vert}} = \\ & = 2 \left( (Q^2 + 2m_e^2) L_m - 1 \right) \ln \left( \frac{v_{\text{cut}}}{m_e M_d} \right) + \\ & + \frac{1}{2} (S L_S + X L_X) + S_\phi(k_1, k_2, p_2) + \\ & + \left( \frac{3}{2} Q^2 + 4m_e^2 \right) L_m - 2 - \frac{(Q^2 + 2m_e^2)}{\sqrt{\lambda_m}} \times \\ & \times \left( \frac{1}{2} \lambda_m L_m^2 + 2 \text{Li}_2 \left( \frac{2\sqrt{\lambda_m}}{Q^2 + \sqrt{\lambda_m}} \right) - \frac{\pi^2}{2} \right), \quad (33) \end{aligned}$$

where

$$\begin{aligned} L_m &= \frac{1}{\sqrt{\lambda_m}} \ln \left( \frac{\sqrt{\lambda_m} + Q^2}{\sqrt{\lambda_m} - Q^2} \right), \\ L_S &= \frac{1}{\sqrt{\lambda_S}} \ln \left( \frac{S + \sqrt{\lambda_S}}{S - \sqrt{\lambda_S}} \right), \\ L_X &= \frac{1}{\sqrt{\lambda_X}} \ln \left( \frac{X + \sqrt{\lambda_X}}{X - \sqrt{\lambda_X}} \right), \\ \lambda_X &= X^2 - 4m_e^2 M_d^2. \quad (34) \end{aligned}$$

The functional form  $S_\phi(k_1, k_2, p_2)$  is given by

$$\begin{aligned} S_\phi(k_1, k_2, p_2) = & \frac{Q^2 + 2m_e^2}{\sqrt{\lambda_m}} \left( \frac{1}{4} \lambda_X L_X^2 - \frac{1}{4} \lambda_S L_S^2 + \right. \\ & + \text{Li}_2 \left[ 1 - \frac{(X + \sqrt{\lambda_X}) T}{8m_e^2 M_d^2} \right] + \text{Li}_2 \left[ 1 - \frac{T}{2(X + \sqrt{\lambda_X})} \right] - \\ & - \text{Li}_2 \left[ 1 - \frac{Q^2 (S + \sqrt{\lambda_S}) T}{2M_d^2 (Q^2 + \sqrt{\lambda_m})^2} \right] - \\ & \left. - \text{Li}_2 \left[ 1 - \frac{2m_e^2 Q^2 T}{(Q^2 + \sqrt{\lambda_m})^2 (S + \sqrt{\lambda_S})} \right] \right), \quad (35) \end{aligned}$$

where

$$\begin{aligned} X &= S - Q^2, \\ T &= \frac{(Q^2 + \sqrt{\lambda_m})(S_p - \sqrt{\lambda_m})}{\sqrt{\lambda_m}}, \\ S_p &= S + X = 2S - Q^2, \end{aligned} \quad (36)$$

and  $\text{Li}_2$  is Spence's dilogarithmic function

$$\text{Li}_2(x) = - \int_0^x \frac{\ln|1-y|}{y} dy. \quad (37)$$

Thus, we have  $\delta_{VR}(Q^2)$  in Eq. (33), and the term  $\delta_{VR}(\theta_e)$  is calculated using Eq. (23).

• **RC term  $\delta_{\text{vac}}^l$ .** In the panel (b) of Fig. 2, the diagram of vacuum polarization is depicted. In this case,  $\delta_{\text{vac}}^l$  is the leptonic vacuum polarization correction to the electric Dirac form factor of the electromagnetic vertex; namely, the polarization originated by  $e$ ,  $\mu$ , and  $\tau$  charged leptons:

$$\delta_{\text{vac}}^l(Q^2) = \sum_{i=e,\mu,\tau} \delta_{\text{vac}}^{l,i} = \sum_{i=e,\mu,\tau} \left( \frac{2}{3} (Q^2 + 2m_i^2) L_m^i - \frac{10}{9} + \frac{8m_i^2}{3Q^2} (1 - 2m_i^2 L_m^i) \right), \quad (38)$$

where  $L_m^i$  is defined as

$$L_m^i = \frac{1}{\sqrt{\lambda_m^i}} \ln \left( \frac{\sqrt{\lambda_m^i} + Q^2}{\sqrt{\lambda_m^i} - Q^2} \right), \quad (39)$$

with

$$\lambda_m^i = Q^2 (Q^2 + 4m_i^2), \quad (40)$$

being exactly the same as Eq. (21) and the first formula of Eq. (34) but both applied to the three lepton species here.

In this case, we have  $\delta_{\text{vac}}^l(Q^2)$  in Eq. (38), and the term  $\delta_{\text{vac}}^l(\theta_e)$  is calculated using Eq. (23).

• **RC term  $\delta_{\text{vac}}^h$ .**  $\delta_{\text{vac}}^h$  is the vacuum polarization correction by hadrons to the electric Dirac form factor of the electromagnetic vertex, taken as a fit to experimental cross section data (via dispersion relations) for  $e^+e^-$  annihilation to hadrons. In our RC framework, we use a parametrization [46, 88]

$$\delta_{\text{vac}}^h(Q^2) = -\frac{2\pi}{\alpha} [\Delta + \Xi \log(1 + \Sigma Q^2)], \quad (41)$$

where the fit parameters  $\Delta$ ,  $\Xi$  and  $\Sigma$  are shown in Table 1. The hadronic polarization contribution is actually quite small at very low  $Q^2$  as compared to all-leptonic polarization contribution, which is computed in [37] based on using the Fortran package `alphaQED` of F. Jegerlehner [91].

We have  $\delta_{\text{vac}}^h(Q^2)$  in Eq. (41), and the term  $\delta_{\text{vac}}^h(\theta_e)$  is calculated using Eq. (23).

$ t , (\text{GeV}/c)^2$	$\Delta$	$\Xi$	$\Sigma$
0 – 1	$-1.345 \times 10^{-9}$	$-2.302 \times 10^{-3}$	4.091

**Table 1** The values of the three parameters in Eq. (41), shown in a given range of  $|t| = Q^2$ . The parameters in larger  $|t|$  ranges can be seen in Table 1 of [88].

• **RC term  $\delta_{\text{inf}}$ .** As a first approximation, contributions of higher-order RCs are taken into consideration by an exponentiation procedure in accordance with [71] (see also [36, 45]). This procedure simply accounts for multiple soft photons and corresponding loops for canceling the infrared divergences. Then the term designated by  $\delta_{\text{inf}}$  is used to account for multi-photon radiation at  $Q^2 \rightarrow 0$ :

$$\delta_{\text{inf}}(Q^2) = (Q_m^2 L_m - 1) \ln \left( \frac{v_{\text{cut}}^2}{S(S - Q^2)} \right). \quad (42)$$

The exponentiation procedure is manifested by the  $e^{(\alpha/\pi)\delta_{\text{inf}}}$  term, which stands in the observed cross section (see Eq. (28) and Eq. (29)).

We have  $\delta_{\text{inf}}(Q^2)$  in Eq. (42), and the term  $\delta_{\text{inf}}(\theta_e)$  is calculated using Eq. (23).

• **Cross-section terms  $d\sigma^{\text{AMM}}/dQ^2$  and  $d\sigma^{\text{AMM}}/d\theta_e$ .** There is also the anomalous magnetic moment's contribution to the cross section, which stems from the leptonic vertex correction:

$$\begin{aligned} \frac{d\sigma^{\text{AMM}}}{dQ^2} &= \frac{\alpha^3 m_e^2 L_m}{2M_d^2 Q^2 \lambda_S} \times \\ &\times \left( 12M_d^2 W_{1d}(Q^2) - (Q^2 + 4M_d^2) W_{2d}(Q^2) \right), \end{aligned} \quad (43)$$

where the functions  $W_{1d}(Q^2)$  and  $W_{2d}(Q^2)$  are shown in Eq. (B4) and Eq. (B5), respectively. The term  $d\sigma^{\text{AMM}}/d\theta_e$  should be determined from

$$\frac{d\sigma^{\text{AMM}}}{dQ^2} = -\frac{1}{j_\theta \sin(\theta_e)} \frac{d\sigma^{\text{AMM}}}{d\theta_e}, \quad (44)$$

• **Cross-section terms  $d\sigma_R^F/dQ^2$  and  $d\sigma_R^F/d\theta_e$ .** The last ingredient of the unpolarized  $e - d$  elastic scattering cross section is the infrared-free contribution  $d\sigma_R^F$  from Eq. (30). In this case, for convenience of calculations of the cross section, the matrix element squared in Eq. (17) can be represented as

$$\begin{aligned} \mathcal{M}_R^2 &= \frac{(4\pi\alpha)^3}{\tilde{Q}^4} \times \\ &\times L_R^{\mu\nu} \left( \tilde{w}_{\mu\nu}^1 W_{1d}(\tilde{Q}^2) + \tilde{w}_{\mu\nu}^2 W_{2d}(\tilde{Q}^2) \right), \end{aligned} \quad (45)$$

where the coefficients  $w_{\mu\nu}^i$  and the functional forms  $W_{id}$  are explicitly shown in Eqs. (B3)-(B5). For the radiative leptonic tensor  $L_R^{\mu\nu}$ , see the equations (50) and (51) in [52]. The symbol ‘‘tilde’’ means that  $Q^2$  is defined via the shifted

$q \rightarrow (q - k)$ , i.e., by the following replacement of the argument:

$$\tilde{Q}^2 = -(q - k)^2 = Q^2 + R\tau. \quad (46)$$

The tensor contraction  $L_R^{\mu\nu} \tilde{w}_{\mu\nu}^i$  can be expanded in powers of  $R$  via a convolution integral that is given by the equation (52) in [52].

In order to compute  $\sigma_R^F$ , one can actually integrate  $\sigma_R$  over  $\phi_k$  analytically, and then the integration should be performed over the  $\tau$  variable<sup>5</sup>. After the infrared divergence extraction, the resulting expression is integrated over  $v$ . Eventually, the finalized finite part of the cross section as a function of  $Q^2$  reads as

$$\begin{aligned} \frac{d\sigma_R^F}{dQ^2} = & -\frac{\alpha^3}{2\lambda_S} \int_0^{v_{\text{cut}}} dv \sum_{i=1}^2 \left[ 4 \frac{J_0 \theta_B^i W_{id}(Q^2)}{v Q^4} + \right. \\ & \left. + \int_{\tau_q^{\text{min}}}^{\tau_q^{\text{max}}} \frac{d\tau}{(1+\tau) \tilde{Q}^4} \sum_{j=1}^{k_i} W_{id}(\tilde{Q}^2) R^{j-2} \theta_{ij}(v, \tau, Q^2) \right], \end{aligned} \quad (47)$$

in which  $k_i = \{3, 4\}$ . For the three-variable function  $\theta_{ij}$ , see the equations (53)-(55) in [52], however, where  $M$  must be substituted by  $M_d$ . The limits  $\tau_q^{\text{min}}$  and  $\tau_q^{\text{max}}$  at fixed  $Q^2$  are obtained to be

$$\tau_q^{\text{max,min}} = \frac{v + Q^2 \pm \sqrt{\lambda_q}}{2M_d^2}, \quad (48)$$

where  $\lambda_q$  is given by

$$\lambda_q = (v + Q^2)^2 + 4M_d^2 Q^2. \quad (49)$$

Besides,  $J_0$  is represented by

$$J_0 = 2((Q^2 + 2m_e^2) L_m - 1), \quad (50)$$

and  $\theta_B^i$  is given by Eq. (B7).

In the case of the finite part of the cross section as a function of  $\theta_e$ , we have

$$\begin{aligned} \frac{d\sigma_R^F}{d\theta_e} = & \sin(\theta_e) \times \left( \frac{\alpha^3}{2\lambda_S} \right) \times \\ & \times \int_0^{v_{\text{cut}}} dv \sum_{i=1}^2 \left[ 4j_\theta \frac{J_0 \theta_B^i W_{id}(Q^2)}{v Q^4} + \right. \\ & \left. + J_\theta(v) \int_{\tau_\theta^{\text{min}}}^{\tau_\theta^{\text{max}}} \frac{d\tau}{(1+\tau) \tilde{Q}^4} \times \right. \\ & \left. \times \sum_{j=1}^{k_i} W_{id}(\tilde{Q}^2) R^{j-2} \theta_{ij}(v, \tau, Q_R^2(v)) \right], \end{aligned} \quad (51)$$

<sup>5</sup>The integral of  $d\sigma_R^F/d\Omega$  is given by Eq. (43) in [36].

in which

$$\tau_\theta^{\text{max,min}} = \frac{v + Q_R^2(v) \pm \sqrt{\lambda_v}}{2M_d^2}, \quad (52)$$

and where

$$\lambda_v = (v + Q_R^2(v))^2 + 4M_d^2 Q_R^2(v), \quad (53)$$

$$\begin{aligned} Q_R^2(v) = & \frac{1}{(S + 2M_d^2)^2 - \lambda_S \cos^2(\theta_e)} \times \\ & \times \left( (S + 2M_d^2) (\lambda_S - vS) - \lambda_S (S - v) \cos^2(\theta_e) - \right. \\ & \left. - 2M_d \sqrt{\lambda_S} \sqrt{\mathcal{D}} \cos(\theta_e) \right), \end{aligned} \quad (54)$$

$$\begin{aligned} \mathcal{D} = & M_d^2 (\lambda_S + v(v - 2S)) - \\ & - m_e^2 (\lambda_S \sin^2(\theta_e) + 4vM_d^2). \end{aligned} \quad (55)$$

Also,

$$\begin{aligned} J_\theta(v) = & -\frac{\lambda_S - vS - Q_R^2(v) (S + 2M_d^2)}{(S + 2M_d^2)^2 - \lambda_S \cos^2(\theta_e)} \times \\ & \times \left( \frac{S + 2M_d^2}{\cos(\theta_e)} + M_d \sqrt{\frac{\lambda_S}{\mathcal{D}}} (S - v + 2m_e^2) \right), \end{aligned} \quad (56)$$

and  $j_\theta \equiv J_\theta(0)$ .

Again, as in all the previous cases,  $Q^2$  in Eq. (51) should be transformed to  $\theta_e$  using Eq. (23).

## 4 Numerical results

In order to produce the figures shown in this section, we have used an event generator for unpolarized elastic  $e - d$  scattering with hard radiative photons. That generator, a.k.a. DRad e-d is developed recently [92] based on the PRad event generator located within the PRad analyzer package [93]. This package has already been successfully utilized for monitoring and analyzing the PRad experimental data [87], and the event generator there has been built based on the cross sections including the  $e - p$  and Møller lowest-order RCs calculated in Ref. [36].

For a consistency check, some of the numerical results produced from the DRad event generator are compared to those produced from the MASSRAD package that can be found in [94]. In this section, we show several numerical results (for the DRad kinematics) on the lowest-order RCs, obtained from cross sections and related formulas discussed in the previous sections, as well as in Appendix A and Appendix B.



#### 4.1 The numerical behavior of the unpolarized elastic $e - d$ cross section

Two inelasticity cut-off values,  $v_{\text{cut}}$  and  $v_{\text{min}}$ , are considered in the calculations here, where we have  $v_{\text{min}} \leq v_{\text{cut}} \leq v_{q,\theta}^{\text{max}}$ , with  $v_q^{\text{max}}$  shown in Eq. (22), though  $v_{\theta}^{\text{max}}$  is represented by the same formula too [52].  $v_{\text{cut}}$  is an experimental quantity that can be considered as the upper limit of Bremsstrahlung integration, being an inelasticity cut-off value for performing calculations in the range of interest. It is large enough to account for radiative tail effects. In our calculations, we accept  $v_{\text{cut}} = 3.9 \text{ GeV}^2$  and  $v_{\text{cut}} = 8.1 \text{ GeV}^2$  that correspond to a 1050 MeV radiative photon at 1.1 GeV beam energy and a 2150 MeV radiative photon at 2.2 GeV beam energy, respectively.  $v_{\text{min}}$  is an arbitrary value for separating the Bremsstrahlung region into soft (non-radiative) and hard (radiative) parts. As  $v_{\text{min}}$  corresponds to the minimal energy of a radiative photon that can be detected, a requirement on  $v_{\text{min}}$  must be abided such that it is less than the resolution of the HyCal<sup>6</sup> ( $\Delta E = 2.6\% \times \sqrt{E_1}$ , with  $E_1$  given in GeV). The effect of selecting different  $v_{\text{min}}$  values is discussed in this section as well.

For the purpose of convenience and effectiveness of numerical simulations, the observed cross section of the unpolarized elastic  $e - d$  scattering as a function of  $Q^2$  and  $\theta_e$  given by Eq. (28) and Eq. (29) is divided into the aforementioned soft and hard parts in the DRad event generator of [92]. The cross section with the soft part of the lowest-order RCs and without any RCs is shown in Fig. 3. The DRad kinematic range is used for the four-momentum transfer squared and the electron scattering angle:

$$Q^2 = 2 \times 10^{-4} (\text{GeV}/c)^2 - 5 \times 10^{-2} (\text{GeV}/c)^2,$$

and

$$\theta_e = 0.7^\circ - 6.0^\circ.$$

So in Fig. 3, the notation  $\sigma$  in the vertical axis should be understood as  $\sigma^B$  and  $\sigma^{\text{soft}}$ . The Born cross section (solid lines) is computed from Eq. (7) and Eq. (24). The cross section with the soft RCs is shown as dot-dashed lines. Namely, the cross section  $d\sigma^{\text{soft}}/d\theta_e$  is computed from Eq. (29) while using  $v_{\text{min}} = 2 \times 10^{-4} \text{ GeV}^2$ . The cross section  $d\sigma^{\text{soft}}/dQ^2$  in turn is computed from Eq. (28) while the applied  $v_{\text{min}}$  is set to be larger because of some complications in the numerical integration, used as  $v_{\text{min}} = 1 \times 10^{-3} \text{ GeV}^2$  at 1.1 GeV and  $v_{\text{min}} = 3 \times 10^{-3} \text{ GeV}^2$  at 2.2 GeV.

The soft part of the lowest-order RCs as a function of  $\theta_e$  and  $Q^2$  can be quantified by the following formulas:

$$\delta_{ed} = \left( \frac{d\sigma^{\text{soft}}}{d\theta_e} \bigg/ \frac{d\sigma^B}{d\theta_e} \right) - 1, \quad (57)$$

<sup>6</sup>The HyCal is a hybrid electromagnetic calorimeter in the PRad experimental setup for detecting energies and scattering angles of electrons from both elastic  $e-p$  and Møller ( $e-e$ ) scatterings. An upgraded HyCal has been proposed for deployment in the PRad-II [33] and DRad experimental setups.

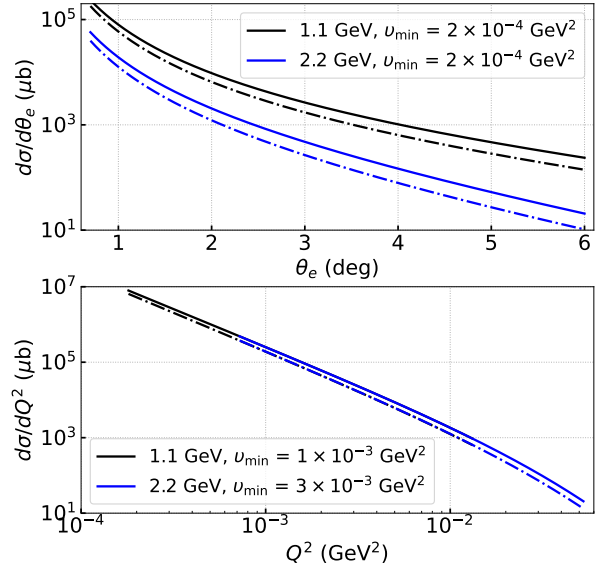


**Fig. 3** (Color online) The observed cross section in the unpolarized elastic  $e - d$  scattering as a function of  $\theta_e$  (top panel) and  $Q^2$  (bottom panel) at  $E_1 = 1.1 \text{ GeV}$  and  $2.2 \text{ GeV}$  electron beam energies. The solid lines describe the Born cross section calculated from Eqs. (7) and (24). The dot-dashed lines describe the cross sections with the soft part of the lowest-order radiative corrections, calculated from Eqs. (29) and (28), and based upon using the Abbott1 form-factor model in Eq. (A1).

and

$$\delta_{ed} = \left( \frac{d\sigma^{\text{soft}}}{dQ^2} \bigg/ \frac{d\sigma^B}{dQ^2} \right) - 1, \quad (58)$$

Thereby,  $\delta_{ed}$  is defined as the relative difference between the soft and Born differential cross sections. Then the upper panel in Fig. 4 shows the lowest-order RCs quantified by  $\delta_{ed}$  as a function of  $Q^2$  for different values of  $v_{\text{min}}$  and for beam energies at  $E_1 = 1.1 \text{ GeV}$  and  $2.2 \text{ GeV}$ , produced using the form-factor Abbott1 model (see Parametrization I (Abbott1 model) in Appendix A).

Here we emphasize the importance of using the electron mass in the formulas derived in Sec. 3.2. In an extremely low  $Q^2$  range, the ultra-relativistic approximation is not suitable and therefore not used in this work. Nonetheless, one can estimate that at  $Q^2 \sim 10^{-4} \text{ GeV}^2$ , the term  $4m_e^2 \sim 10^{-6} \text{ GeV}^2$  contributes to 1% for  $\lambda_m$  in Eq. (21). In turn,  $\lambda_m$  enters in the formula of  $L_m$  in Eq. (34) (also, in Eq. (33) or, in Eq. (35) directly) that stands in all the terms in Eq. (28) (and in Eq. (29)) except for  $\delta_{\text{vac}}^h$ . Corrections to the differential cross section are roughly proportional to  $L \equiv \ln(Q^2/m_e^2)$  (see, e.g, Eq. (61) to be discussed a bit later). This  $L$  is not the same as  $L_m$ , however, both have a similar behavior. One can think of the cross section in Eq. (28) to behave roughly linearly with  $L_m$ . In this case, the effect due to the electron mass in Eq. (28) (or, in Eq. (29)), namely, between the same cross section but beyond and within ultra-relativistic approximation, may be considered to be at the level of 1%.

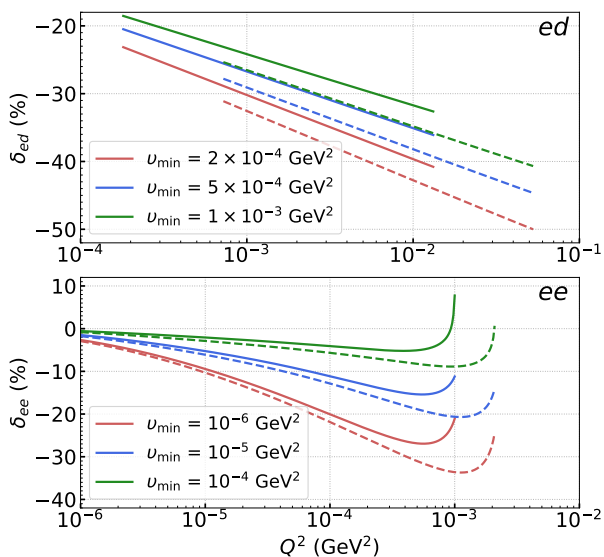


**Fig. 4** (Color online) (Top panel) Lowest-order radiative effects in the unpolarized elastic  $e-d$  scattering process. The solid curves represent  $\delta_{ed}$  at  $E_1 = 1.1$  GeV, and the dashed lines represent it at  $E_1 = 2.2$  GeV. The Abbott1 form-factor model in Eq. (A1) is used in the calculations of  $\delta_{ed}$  curves. (Bottom panel) Radiative effects described by  $\delta_{ee}$  for the Møller process, with the same definition. Different ranges for parameters and  $Q^2$  are chosen according to the kinematics of these two processes within the DRad experimental acceptance. The values of  $v_{\min}$  and  $Q^2$  are chosen according to the kinematics coverage of the DRad experiment for each process.

During the PRad data taking that happened in 2016, the luminosity was monitored by simultaneously measuring the Møller process, and the absolute cross section was normalized to that of the Møller process to have some level of control of systematics. The same technique will be utilized in the PRad-II and DRad experiments. In this respect, it is relevant to show a similar to  $\delta_{ed}$  definition that quantifies the ( $Q^2$ -dependent) Møller RCs:

$$\delta_{ee} = \left( \frac{d\sigma_{ee}^{\text{soft}}}{dQ^2} \bigg/ \frac{d\sigma_{ee}^B}{dQ^2} \right) - 1. \quad (59)$$

The bottom plot in Fig. 4 shows examples of this quantity  $\delta_{ee}$ , which is produced using the PRad event generator in [93].

As expected, the smaller the value of  $v_{\min}$  is selected, the larger the values of  $\delta_{ed}$  and  $\delta_{ee}$  are obtained because  $\delta_{ed}$  is dominated by  $\delta_{VR}$  (see Eq. (33)) in the soft region. However, only the events within the elastic window will be selected in our future data analysis. In this window, the total size of the lowest-order RCs in the unpolarized elastic  $e-d$  cross section can be given by the following formula:

$$\mathcal{R}_{ed} = (\sigma^{\text{obs}}/\sigma^B) - 1, \quad (60)$$

where  $\sigma^{\text{obs}}$  and  $\sigma^B$  are integrated cross sections.  $\mathcal{R}_{ed}$  is defined as the relative difference between the observed and Born cross sections integrated over the DRad acceptance

and within an energy (elasticity) cut. In Fig. 5, we show the normalized distribution of  $e-d$  events with hard radiative photons simulated by the DRad generator at 1.1 GeV. The dashed band describes the elastic  $e-d$  region of interest (ROI) from the  $4\text{-}\sigma_E$  energy cut in the HyCal. The inset shows  $\mathcal{R}_{ed}$  as a function of  $v_{\min}$  within the range from  $2 \times 10^{-4}$  GeV<sup>2</sup> to  $2 \times 10^{-2}$  GeV<sup>2</sup>. Every point is calculated using  $10^7$  simulated events. In the ROI,  $\mathcal{R}_{ed}$  is very stable (and within the statistical uncertainty 0.03%), being 4.2% at 1.1 GeV and 6.9% at 2.2 GeV.

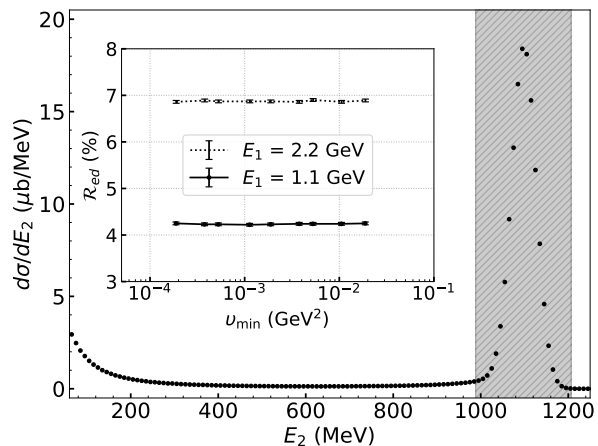


**Fig. 5** The cross section  $d\sigma/dE_2$  for the elastic  $e-d$  process at  $E_1 = 1.1$  GeV and within  $0.7^\circ < \theta_e < 6.0^\circ$ . The spectrum includes radiative effects and is smeared by the HyCal resolution of  $\Delta E = 2.6\% \times \sqrt{E_1}$ . The elasticity cut of  $4\text{-}\sigma_E$  is shown by the shaded area. The inset shows the experimental radiative effects  $\mathcal{R}_{ed}$ . With a reasonably small  $v_{\min}$ , the calculated radiative effects under the elastic peak are independent of the choice of this parameter.

All the results shown in this Sec. 4.1 on  $e-d$  scattering are generated by using the Abbott1 form-factor model. However, the effect coming from the other form-factors models (discussed in Appendix A) is also studied. As shown in Fig. 6, the difference in the relative radiative correction due to different form-factor models is negligible, being less than 0.01%. Although the bin-by-bin observed and Born cross sections due to the other three form-factor models differ by up to 0.15% from the Abbott1 model.

#### 4.2 Estimation of higher-order RC systematic uncertainty on $r_d$ for the DRad experiment

Ref. [37] discusses QED RC corrections to elastic  $e-p$  scattering at low energies. In its treatment, higher-order corrections relevant to high-precision experiments are presented in an analytic form. The method of [37] has been used by PRad but is kind of simplified for estimating the RC systematic uncertainty on the measured  $r_p$ . In this section, we use the same procedure but for the elastic  $e-d$  scattering to esti-

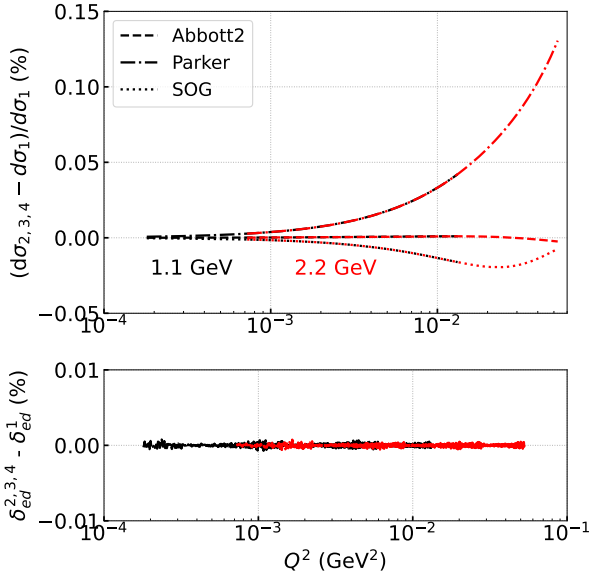


**Fig. 6** (Top panel) The relative difference of the cross sections between the Abbott2, Parker and SOG form-factor models,  $d\sigma_{2,3,4}$ , and the Abbott1 model,  $d\sigma_1$ . (Bottom panel) The residual of  $\delta_{ed}$  between the other form-factor models,  $\delta_{ed}^{2,3,4}$ , and the Abbott1 model,  $\delta_{ed}^1$ . The applied  $v_{\min}$  is  $2 \times 10^{-4} \text{ GeV}^2$ .

mate the RC systematic uncertainty on  $r_d$  for the kinematics of the DRad experiment.

So, as discussed in equation (2) of [37], a typical  $\mathcal{O}(\alpha)$  correction to the differential cross section is at the magnitude of

$$\delta^{(1)} = \frac{d\sigma^{(1)}}{d\sigma^{(0)}} \sim \alpha(a \times L + b), \quad (61)$$

where  $\alpha$  is the electromagnetic fine-structure constant,  $a$  and  $b$  are some constants,  $L \equiv \ln(Q^2/m_e^2)$  is the so-called large logarithm. Then the approximate next-to-next-leading order (NNLO)  $\mathcal{O}(\alpha^2 L^1)$  corrections can be calculated by a power counting method. From Eq. (33) and Eq. (38), one can write down

$$\delta_{VR} + \delta_{\text{vac}}^l \sim \alpha(a_{VR} \times L + b_{VR}), \quad (62)$$

with

$$\begin{aligned} a_{VR} &= \frac{3}{2} + \frac{2}{3}, \\ b_{VR} &= -2 - \frac{1}{2} \ln\left(\frac{S}{S-Q^2}\right)^2 + \\ &\quad + \text{Li}_2\left(\frac{M_d^2 Q^2}{S(S-Q^2)}\right) - \frac{\pi^2}{6} - \frac{10}{9}. \end{aligned} \quad (63)$$

From Eq. (42), we also obtain

$$\delta_{\text{inf}} \sim \alpha(a_{\text{inf}} \times L + b_{\text{inf}}), \quad (64)$$

with

$$\begin{aligned} a_{\text{inf}} &= \ln\left(\frac{v_{\text{max}}^2}{S(S-Q^2)}\right), \\ b_{\text{inf}} &= -\ln\left(\frac{v_{\text{max}}^2}{S(S-Q^2)}\right). \end{aligned} \quad (65)$$

As a result, the higher-order RCs originate from the interference between the terms in Eq. (62) and Eq. (64):

$$\begin{aligned} \delta^{(2)} &= \frac{d\sigma^{(2)}}{d\sigma^{(0)}} \sim \\ &\sim \alpha^2 L(a_{VR} \times b_{\text{inf}} + b_{VR} \times a_{\text{inf}} + a_{\text{inf}} \times b_{\text{inf}}). \end{aligned} \quad (66)$$

Note that the term  $a_{VR} \times b_{VR}$  is of the order of  $\mathcal{O}(\alpha^2 L^2)$ . Ultimately, in the DRad kinematic range, we treat the bin-by-bin  $\delta^{(2)}$  as the higher-order RC relative systematic uncertainty imposed on  $r_d$ , which is

$$0.06\% \sim 0.10\% \quad \text{at } E_1 = 1.1 \text{ GeV beam energy,}$$

and

$$0.10\% \sim 0.15\% \quad \text{at } E_1 = 2.2 \text{ GeV beam energy.}$$

## Summary and outlook

In this paper, we presented numerical results from the lowest-order QED radiative correction calculations for the unpolarized elastic  $e-d$  scattering, by making use of the available four deuteron electromagnetic elastic form-factor models. We carried out the calculations within a covariant formalism, whereby the derived cross-section formulas may be directly applied to any coordinate system. Besides, we obtained our results beyond the ultra-relativistic approximation, which means that the electron mass is not neglected in the final expressions. This approximation is no more appropriate in the considered kinematics since the calculated RCs are necessary for the deuteron cross-section and charge-radius measurements that will be accomplished at very low- $Q^2$  region in the DRad experiment at Jefferson Lab. As such, we also presented our estimation of the bin-by-bin RC relative systematic uncertainty on the deuteron charge radius  $r_d$  due to higher-order effects.

Our framework is anchored upon the Bardin-Shumeiko technique applied to the infrared-divergence extraction and cancellation, which has been previously used in Refs. [36, 45–50, 52, 53] for unpolarized elastic  $e-p$  and Møller cross-section computations with the lowest-order RCs, as well as for semi-inclusive DIS cross-section computations again including the lowest-order RCs.

Besides, we do not discuss the hadronic bremsstrahlung and/or vertex correction to the hadronic current (deuteron leg) based on the following considerations.

- (i) First, in our calculations we consider RCs to the leptonic current that include real photon radiation from the leptonic leg and vertex, plus also photon self energy. These effects may be calculated without any assumption on hadron interactions, and represent the so-called model-independent RC contribution. It is the largest contribution to the total RC and can be computed exactly or in the leading-log approximation, if the accuracy provided

by this approximation is sufficient. By “exactly” computing the RCs, we understand analytic expressions obtained without any simplified assumption, by having also opportunities for numeric estimates with any predetermined accuracy.

- (ii) Second, the uncertainties of the model-independent RC contribution come only from fits and data related to structure functions, whereas the model-dependent corrections (i. e., box-type diagrams, radiation by hadronic leg and hadronic vertex) require additional information on the hadron interactions, and therefore may contain additional purely theoretical uncertainties, which are not easy to control.
- (iii) Another reason is that  $m_e \ll M_d$ , which may result in the hard photon radiation probability from the deuteron to be insignificant, thus giving negligible contribution to the total cross section.

In our approach to the RC treatment, we currently do not consider the two-photon exchange (TPE) box diagrams either. The reason is that the hard photon’s radiation probability from the deuteron is very low because of  $M_d \gg m_e$ . Also, the form-factor parametrizations we used come from data that had not been corrected for the TPE exchange. This means that the TPE effect should be partially included in our results, being nested in the deuteron elastic form-factors. Consequently, a possible double counting would be performed in calculations of the box diagram and hard photon radiation. By stating “partially included”, we consider the fact that the TPE effects are in general non-linear with the scattering-angle parameter  $\varepsilon$  (transverse virtual photon polarization), given by

$$\varepsilon = \frac{1}{1 + 2(1 + \eta) \tan^2(\theta/2)}, \quad \text{with } \eta = \frac{Q^2}{4M_d^2}, \quad (67)$$

while the cross section is linear with respect to  $\varepsilon$  for the Born approximation.

Although, important enough pertinent to our case is that the effect of TPE corrections have already been studied and determined to be negligible in the kinematics of the PRad experiment. Two  $e - p$  event generators used in the PRad simulations [87] for the purpose of  $r_p$  extraction incorporated the contribution from the TPE processes studied in [95–97]. That contribution was estimated to be less than 0.2% of the elastic  $e - p$  scattering cross section in the given PRad kinematic range. Moreover, the cross-section sensitivity to two sets of TPE corrections was investigated within the dispersion theoretical framework for elastic  $e - p$  and  $e^+ + p$  scattering [98], resulting in these corrections to be rather small at the PRad/PRad-II beam energies. The TPE corrections for  $e - d$  scattering have been discussed in [99–101] but in much higher  $Q^2$  ranges. As indicated in [101], such corrections on the deuteron form factors extracted from  $e - d$  scattering are expected to be dominated

by the TPE effects on the nucleon form factors determined from electron-nucleon scattering. Therefore, for DRad one can expect a small contribution of TPE as in PRad (at least on the lowest-order RC level), inasmuch as its kinematics is very close to that of PRad/PRad-II.

On the other hand, the TPE corrections in elastic  $e - d$  scattering at low  $Q^2$  could be different from those of  $e - p$  scattering due to the presence of the deuteron quasielastic breakup channel in the former case, which is an intermediate state in the TPE amplitude. Perhaps one needs to compute this contribution, including the distortion that arises from the strong interactions in the  $pn$  intermediate state close to the deuteron threshold [102]. Ultimately, if it turns out that the TPE corrections are not negligible in elastic  $e - d$  scattering at low  $Q^2$  after the TPE theory and/or measurements produce new results, then that contribution may be independently added to our present and future cross-section calculations.

It should also be noted that we have only an approximate treatment of higher-order RC effects in our current ansatz. Nevertheless, in the near- or mid-term future, it may be important to perform state-of-the-art calculations of the NNLO and two-loop irreducible RC contributions for the unpolarized elastic  $e - d$  scattering process<sup>7</sup>. In that case, the RC component of the total systematic uncertainty on  $r_d$  could be much smaller than what is estimated in Sec. 4.2. We currently work on developing our approach for such higher-order RC calculations in the unpolarized elastic  $e - p$  scattering (including the box diagrams too, for computing the TPE corrections), which means that such developments may be well applied to the case of  $e - d$ . Furthermore, similar higher-order RC results and quite elaborately-developed frameworks for lepton-proton scattering in Ref. [56] and Ref. [59], though made for other experiments and kinematics, may likewise be employed by the PRad collaboration in using them in the DRad experiment [44].

## Acknowledgments

The work of J. Z., V. K., and H. G. is supported in part by the U.S. Department of Energy, Office of Science, Office of Nuclear Physics under contract DE-FG02-03ER41231. The work of C. P. is supported in part by the same as above but under contract DE-AC05-06OR23177. S. S. is supported in part by Brookhaven National Laboratory LDRD 21-045S. W. X. is supported by the Shandong Province Natural Science Foundation under grant No. 2023HWYQ-010.

<sup>7</sup>Before starting calculations of the NNLO irreducible contributions, we may first perform reducible two-loop and quadratic calculations. The quadratic part appears in the two-loop correction that stems from the square of one-loop amplitudes [65].

## Data Availability Statement

This manuscript has no associated data or the data will not be deposited. [Authors' comment: This is a theoretical study and it has no associated experimental data.]

## Appendix A: Deuteron elastic form-factor models

Let us now concisely discuss parametrizations describing the available form-factor models: namely Abbott1, Abbott2, Parker, and SOG (Sum-of-Gaussian) with given functional forms of  $G_C^d$ ,  $G_M^d$ , and  $G_Q^d$ <sup>8</sup>. These four models are produced by the fits to the available data in the range from  $Q^2 = 3 \times 10^{-2}$  (GeV/c)<sup>2</sup> to 1.5 (GeV/c)<sup>2</sup>.

(i) Parametrization I (Abbott1 model) [83].

In this first parametrization, the three form factors have a generic form given by

$$G_X^d(Q^2) = G_X^d(0) \times \left[ 1 - \left( \frac{Q}{Q_X^0} \right)^2 \right] \times \left[ 1 + \sum_{i=1}^5 a_{Xi} Q^{2i} \right]^{-1}, \quad (\text{A1})$$

where  $X = C, M$ , and  $Q$ . The corresponding three  $G_X^d(0)$  numbers are normalizing factors fixed by the deuteron static moments. The free parameters  $Q_X^0$  and  $a_{Xi}$  can be found on the websites from [83, 103], and are represented as

$$Q_C^0 = 4.21 \text{ fm}^{-1}; \\ a_{Ci} = 6.740 \cdot 10^{-1}, \quad 2.246 \cdot 10^{-2}, \quad 9.806 \cdot 10^{-3}, \\ -2.709 \cdot 10^{-4}, \quad 3.793 \cdot 10^{-6};$$

$$Q_M^0 = 7.37 \text{ fm}^{-1}; \\ a_{Mi} = 5.804 \cdot 10^{-1}, \quad 8.701 \cdot 10^{-2}, \quad -3.624 \cdot 10^{-3}, \\ 3.448 \cdot 10^{-4}, \quad -2.818 \cdot 10^{-6};$$

$$Q_Q^0 = 8.10 \text{ fm}^{-1}; \\ a_{Qi} = 8.796 \cdot 10^{-1}, \quad -5.656 \cdot 10^{-2}, \quad 1.933 \cdot 10^{-2}, \\ -6.734 \cdot 10^{-4}, \quad 9.438 \cdot 10^{-6}.$$

(ii) Parametrization II (Abbott2 model) [83, 84].

The second parametrization is given by the set of the follow-

ing expressions:

$$G_C^d(Q^2) = \frac{(G(Q^2))^2}{(2\eta + 1)} \left[ \left( 1 - \frac{2}{3}\eta \right) g_{00}^+ + \frac{8}{3} \sqrt{2\eta} g_{+0}^+ + \frac{2}{3} (2\eta - 1) g_{+-}^+ \right], \\ G_M^d(Q^2) = \frac{(G(Q^2))^2}{(2\eta + 1)} \left[ 2g_{00}^+ + \frac{2(2\eta - 1)}{\sqrt{2\eta}} g_{+0}^+ - 2g_{+-}^+ \right], \\ G_Q^d(Q^2) = \frac{(G(Q^2))^2}{(2\eta + 1)} \left[ -g_{00}^+ + \sqrt{\frac{2}{\eta}} g_{+0}^+ - \frac{\eta + 1}{\eta} g_{+-}^+ \right], \quad (\text{A2})$$

where  $G(Q^2)$  is a dipole form factor of the following form:

$$G(Q^2) = \left( 1 + \frac{Q^2}{\delta^2} \right)^{-2}, \quad (\text{A3})$$

with  $\delta$  being a parameter of the order of the nucleon mass  $M_N$ . Besides, we also have

$$g_{00}^+ = \sum_{i=1}^n \frac{a_i}{\alpha_i^2 + Q^2}, \quad g_{+0}^+ = Q \sum_{i=1}^n \frac{b_i}{\beta_i^2 + Q^2}, \\ g_{+-}^+ = Q^2 \sum_{i=1}^n \frac{c_i}{\gamma_i^2 + Q^2}, \quad (\text{A4})$$

in which the sets  $\{a_i, \alpha_i^2\}$ ,  $\{b_i, \beta_i^2\}$ , and  $\{c_i, \gamma_i^2\}$  are fitting parameters. In total, there are twenty-four such parameters, which can be found on the website from [83].

(iii) Parametrization III (Parker model) [103].

Based on the re-fits from the first two parametrizations, the third parametrization has in particular some constraints for handling the singularities in the functional forms of the  $G_C^d$ ,  $G_M^d$  and  $G_Q^d$ :

$$G_X^d(Q^2) = G_X^d(0) \times \left[ 1 - \left( \frac{Q}{Q_X^0} \right)^2 \right] \times \left[ \prod_{i=1}^5 (1 + |b_{Xi}| Q^2) \right]^{-1}, \quad (\text{A5})$$

where  $X = C, M$ , and  $Q$ , along with  $G_X^d(0)$ ,  $Q_X^0$  and  $b_{Xi}$  that have the same meaning as in Eq. (A1). The free parameters  $Q_X^0$  and  $b_{Xi}$  can be found on the websites from [83, 103], and are represented in here as

$$Q_C^0 = 4.21 \text{ fm}^{-1}; \\ b_{Ci} = 2.709 \cdot 10^{-2}, \quad 5.451 \cdot 10^{-1}, \quad 2.709 \cdot 10^{-2}, \\ 2.708 \cdot 10^{-2}, \quad 2.709 \cdot 10^{-2};$$

$$Q_M^0 = 7.37 \text{ fm}^{-1}; \\ b_{Mi} = 3.189 \cdot 10^{-2}, \quad 3.190 \cdot 10^{-2}, \quad 4.433 \cdot 10^{-1}, \\ 3.189 \cdot 10^{-2}, \quad 3.190 \cdot 10^{-2};$$

<sup>8</sup>Ref. [73] has four of the models discussed but only for  $G_C^d$ .

$$\begin{aligned}
Q_Q^0 &= 8.10 \text{ fm}^{-1}; \\
b_{Q_i} &= 4.250 \cdot 10^{-2}, \quad 4.250 \cdot 10^{-2}, \quad 1.347 \cdot 10^{-3}, \\
&4.251 \cdot 10^{-2}, \quad 5.134 \cdot 10^{-1}.
\end{aligned}$$

(iv) Parametrization IV (SOG model) [83, 104, 105].

The fourth parametrization is obtained using the SOG procedure, by which the final generic form of the three form factors read as

$$\begin{aligned}
G_X^d(Q^2) &= \\
&= G_X^d(0) \times e^{-\frac{1}{4}Q^2\gamma^2} \times \sum_{i=1}^N \frac{A_{X_i}}{1 + (2R_{X_i}^2/\gamma^2)} \times \\
&\times \left[ \cos(Q R_{X_i}) + \frac{2R_{X_i}^2}{\gamma^2} \frac{\sin(Q R_{X_i})}{Q R_{X_i}} \right]. \quad (\text{A6})
\end{aligned}$$

where we again have  $X = C, M,$  and  $Q$ . In the coordinate space, in which the parametrization in Eq. (A6) is described better, it corresponds to the  $\rho(R)$  density profile<sup>9</sup>, which is given in terms of a Gaussian sum located at arbitrary radius  $R_{X_i}$ , with amplitudes  $A_{X_i}$  fitted to the three form-factor data sets, given also the fixed Gaussian width  $\gamma = 0.8 \cdot \sqrt{2/3}$  fm. In our fitting procedure, we accept  $N = 12$ . There are free fitting eleven parameters: namely, ten Gaussian amplitudes  $\{A_{X_1}, A_{X_2}, \dots, A_{X_{10}}\}$  at ten points of  $\{R_{X_1}, R_{X_2}, \dots, R_{X_{10}}\} < 4$  fm, respectively. Besides, there is one overall amplitude  $A_{X_{11}}$  corresponding to another  $R_{X_{11}}$  point that is located in the range from 4 fm to 10 fm. For determining the normalization, there is one more amplitude  $A_{X_{12}, \text{norm}}$  taken at the point of  $R_{X_{12}, \text{norm}} = 0.4$  fm. All the given amplitudes satisfy the condition of  $\sum_{i=1}^{12} A_{X_i} = 1$ .

Thereby, to find the parameters  $A_{X_i}$ , we first randomly generate a set of  $R_{X_i}$  in the entire range mentioned above, then fit the functional forms in Eq. (A6) to the  $G_X^d$  data sets from Table 1 of [83] (see also [105]). The sets of  $R_{X_i}$  values are generated repeatedly until the determined  $\chi^2$  value gets minimized and converged. With the eleven fixed  $R_{X_i}$  and eleven free parameters  $A_{X_i}$ , the final fits are obtained [105] to be  $\chi^2/\text{NDF} \simeq 1.625$  for  $G_C^d$ ,  $\chi^2/\text{NDF} \simeq 0.094$  for  $G_M^d$ ,  $\chi^2/\text{NDF} \simeq 1.371$  for  $G_Q^d$ . In this regard, let us represent below all the form-factor fitting parameters and  $R_{X_i}$  values in the SOG model.

$$\begin{aligned}
Q_C^0 &= 4.21 \text{ fm}; \\
A_{C_{1, \dots, C_{11}}} &= 0.072, \quad 236.436, \quad 1454.11, \quad 59.132, \\
&-1052.67, \quad -17.789, \quad -8.492, \quad 995.005, \quad -1323.4, \quad - \\
&365.277, \quad 23.591; \\
A_{C_{12}} &= 1 - \sum_{i=1}^{11} A_{C_i}; \\
r_{1, \dots, 10} &= 2.706, \quad 3.911, \quad 3.831, \quad 1.490, \quad 2.468, \quad 2.838, \\
&1.493, \quad 1.562, \quad 3.863, \quad 3.755 \text{ fm}; \\
r_{11} &= 5.197 \text{ fm};
\end{aligned}$$

<sup>9</sup>The density  $\rho$  is a function of the distance  $R$  between the nucleons and the deuteron center of mass.

$$r_{12} = 4.000 \cdot 10^{-1} \text{ fm};$$

$$\begin{aligned}
Q_M^0 &= 7.37 \text{ fm}; \\
A_{M_{1, \dots, M_{11}}} &= -0.079, \quad -17.805, \quad 1.019, \quad -22.073, \\
&3.337, \quad -147.885, \quad 2.727, \quad -5.093, \quad 28.676, \quad 0.281, \\
&158.688; \\
A_{M_{12}} &= 1 - \sum_{i=1}^{11} A_{M_i}; \\
r_{1, \dots, 10} &= 3.314, \quad 4.413 \cdot 10^{-2}, \quad 3.688, \quad 2.089, \quad 2.332, \\
&3.341, \quad 1.955, \quad 3.725, \quad 5.339 \cdot 10^{-1}, \quad 3.160 \text{ fm}; \\
r_{11} &= 7.008 \text{ fm}; \\
r_{12} &= 4.000 \cdot 10^{-1} \text{ fm};
\end{aligned}$$

$$\begin{aligned}
Q_Q^0 &= 8.10 \text{ fm}; \\
A_{Q_{1, \dots, Q_{11}}} &= 0.359, \quad 3.221, \quad 0.445, \quad -9.954, \quad -7.354, \\
&-247.766, \quad 14.768, \quad -302.738, \quad 548.153, \quad 1.609, \quad - \\
&0.261; \\
A_{Q_{12}} &= 1 - \sum_{i=1}^{11} A_{Q_i}; \\
r_{1, \dots, 10} &= 5.702 \cdot 10^{-1}, \quad 3.987, \quad 2.250, \quad 2.274, \quad 3.596, \\
&2.222, \quad 3.420, \quad 3.731, \quad 1.363, \quad 2.778 \text{ fm}; \\
r_{11} &= 9.511 \text{ fm}; \\
r_{12} &= 4.000 \cdot 10^{-1} \text{ fm}.
\end{aligned}$$

## Appendix B: Born cross section in the ansatz of [52]

In this appendix, following Refs. [52] and [72], we represent the Born cross section of the unpolarized elastic  $e-d$  scattering cross section (see Fig. 1) in the nomenclature of Sec. 3.

The matrix element squared expressed through the convolution of the hadronic and leptonic tensors is given by

$$\mathcal{M}_B^2 = 16\pi^2 \frac{\alpha^2}{Q^4} W_{\mu\nu}(q) L^{\mu\nu}. \quad (\text{B1})$$

The leptonic tensor averaged over the incident unpolarized electron spin and summed over polarizations of the scattered electron has the form of

$$L^{\mu\nu} = q^2 g^{\mu\nu} + 2(k^{1\mu} k^{2\nu} + k^{1\nu} k^{2\mu}). \quad (\text{B2})$$

The hadronic tensor for the unpolarized target and recoil deuterons can be rearranged into the standard covariant form as follows:

$$\begin{aligned}
W_{\mu\nu}(q) &= -\left(g_{\mu\nu} - \frac{q_\mu q_\nu}{q^2}\right) W_{1d}(-q^2) + \\
&+ \frac{1}{M_d^2} \left(p_{1\mu} + \frac{q_\mu}{2}\right) \left(p_{1\nu} + \frac{q_\nu}{2}\right) W_{2d}(-q^2) = \\
&= \sum_{i=1}^2 w_{\mu\nu}^i(q) W_{id}(-q^2), \quad (\text{B3})
\end{aligned}$$

where  $W_{1d}(-q^2)$  and  $W_{2d}(-q^2)$  are directly related to the unpolarized elastic structure functions  $B_d(Q^2)$  and  $A_d(Q^2)$ , respectively, as shown in Eq. (8):

$$W_{1d}(Q^2) = 2M_d^2 B_d(Q^2), \quad (\text{B4})$$

and

$$W_{2d}(Q^2) = 4M_d^2 A_d(Q^2). \quad (\text{B5})$$

Ultimately, after computing the tensor convolution, we can write down the formula of the Born cross section as a function of  $Q^2$  in the one-photon exchange approximation, in the given reference system with the target deuteron at rest:

$$\frac{d\sigma^B}{dQ^2}(E_1, Q^2) = \frac{2\pi\alpha^2}{\lambda_S Q^4} \left( \theta_B^1 W_{1d}(Q^2) + \theta_B^2 W_{2d}(Q^2) \right), \quad (\text{B6})$$

with

$$\theta_B^1 = Q^2 - 2m_e^2, \quad \theta_B^2 = \frac{SX - M_d^2 Q^2}{2M_d^2}. \quad (\text{B7})$$

## References

1. P. J. Mohr, B. N. Taylor and D. B. Newell, Rev. Mod. Phys. **80**, 633 (2008) [arXiv:0801.0028 [physics.atom-ph]]. [1](#)
2. P. J. Mohr, B. N. Taylor and D. B. Newell, Rev. Mod. Phys. **84**, 1527 (2012) [arXiv:1203.5425 [physics.atom-ph]]. [1](#)
3. P. J. Mohr, B. N. Taylor and D. B. Newell, Rev. Mod. Phys. **88**, no. 3, 035009 (2016) [arXiv:1507.07956 [physics.atom-ph]]; J. Phys. & Chem. Ref. Data **45**, 043102 (2016), [https://tsapps.nist.gov/publication/get\\_pdf.cfm?pub\\_id=920686](https://tsapps.nist.gov/publication/get_pdf.cfm?pub_id=920686) [1](#)
4. J. C. Bernauer *et al.* [A1], Phys. Rev. Lett. **105**, 242001 (2010) [arXiv:1007.5076 [nucl-ex]]. [1](#)
5. J. C. Bernauer *et al.* [A1], Phys. Rev. C **90**, no.1, 015206 (2014) [arXiv:1307.6227 [nucl-ex]]. [1](#)
6. X. Zhan, K. Allada, D. S. Armstrong, J. Arrington, W. Bertozzi, W. Boeglin, J. P. Chen, K. Chirapatpimol, S. Choi and E. Chudakov, *et al.* Phys. Lett. B **705**, 59-64 (2011) [arXiv:1102.0318 [nucl-ex]]. [1](#)
7. W. Xiong, A. Gasparian, H. Gao, D. Dutta, M. Khandaker, N. Liyanage, E. Pasyuk, C. Peng, X. Bai and L. Ye, *et al.* Nature **575**, no.7781, 147-150 (2019). [1](#), [2](#), [4](#)
8. M. Mihovilovic, P. Achenbach, T. Beranek, J. Bericic, J. C. Bernauer, R. Böhm, D. Bosnar, M. Cardinali, L. Correa and L. Debenjak, *et al.* Eur. Phys. J. A **57**, no.3, 107 (2021) [arXiv:1905.11182 [nucl-ex]]. [1](#)
9. R. W. Berard, F. R. Buskirk, E. B. Dally, J. N. Dyer, X. K. Maruyama, R. L. Topping and T. J. Traverso, Phys. Lett. **47 B**, 355 (1973). [1](#), [4](#)
10. G. G. Simon, C. Schmitt and V. H. Walther, Nucl. Phys. A **364**, 285 (1981). [1](#), [4](#)
11. S. Platchkov *et al.*, Nucl. Phys. A **510**, 740 (1990). [1](#), [4](#)
12. F. J. Ernst, R. G. Sachs and K. C. Wali, Phys. Rev. **119**, 1105-1114 (1960). [1](#)
13. R. G. Sachs, Phys. Rev. **126**, 2256-2260 (1962). [1](#)
14. J. Arrington, C. D. Roberts and J. M. Zanotti, J. Phys. G **34**, S23-S52 (2007) [arXiv:nucl-th/0611050 [nucl-th]]. [1](#)
15. C. F. Perdrisat, V. Punjabi and M. Vanderhaeghen, Prog. Part. Nucl. Phys. **59**, 694-764 (2007) [arXiv:hep-ph/0612014 [hep-ph]]. [1](#)
16. V. Punjabi, C. F. Perdrisat, M. K. Jones, E. J. Brash and C. E. Carlson, Eur. Phys. J. A **51**, 79 (2015) [arXiv:1503.01452 [nucl-ex]]. [1](#)
17. V. Z. Jankus, Phys. Rev. **102**, 1586 (1956). [1](#)
18. M. Gourdin, Nuov. Cim. **28**, 533 (1963). [1](#)
19. M. Garcon and J. W. Van Orden, Adv. Nucl. Phys. **26**, 293 (2001) [nucl-th/0102049]. [1](#), [3](#), [4](#)
20. Mainz Microtron MAMI [A1 Collaboration], Measurement of the elastic  $A(Q^2)$  form factor of the deuteron at very low momentum transfer and the extraction of the monopole charge radius of the deuteron, (2012), <https://download.uni-mainz.de/fb08-kphal/proposals/MAMI-A1-1-12.pdf> [1](#), [4](#)
21. B. S. Schlimme, P. Achenbach, J. Beričič, R. Böhm, D. Bosnar, L. Correa, M. O. Distler, A. Esser, H. Fonvieille and I. Friščić, *et al.* EPJ Web Conf. **113**, 04017 (2016). [1](#), [4](#)
22. T. B. Hayward and K. A. Griffioen, Nucl. Phys. A **999**, 121767 (2020) [arXiv:1804.09150 [nucl-ex]]. [1](#)
23. R. Pohl *et al.*, Nature (London) **466**, 213 (2010). [2](#)
24. A. Antognini *et al.*, Science **339**, 417 (2013). [2](#)
25. P. J. Mohr, D. B. Newell and B. N. Taylor, Rev. Mod. Phys. **88**, 035009 (2016) [arXiv:1507.07956 [physics.atom-ph]]. [2](#)
26. R. Pohl, R. Gilman, G. A. Miller and K. Pachucki, Ann. Rev. Nucl. Part. Sci. **63**, 175 (2013) [arXiv:1301.0905 [physics.atom-ph]]. [2](#)
27. C. E. Carlson, Prog. Part. Nucl. Phys. **82**, 59 (2015) [arXiv:1502.05314 [hep-ph]]. [2](#)
28. R. J. Hill, EPJ Web Conf. **137**, 01023 (2017) [arXiv:1702.01189 [hep-ph]]. [2](#)
29. A. Beyer *et al.*, Science **358**, 79 (2017). [2](#)
30. N. Bezginov, T. Valdez, M. Horbatsch, A. Marsman, A. C. Vutha, E. A. Hessels, Science **365**, 1007 (2019). [2](#)
31. A. Gasparian (PRad at JLab), EPJ Web Conf. **73**, 07006 (2014). [2](#)
32. C. Peng and H. Gao, EPJ Web Conf. **113**, 03007 (2016). [2](#)
33. A. Gasparian *et al.* [PRad], PRad-II: A New Upgraded High Precision Measurement of the Proton Charge Radius, [arXiv:2009.10510 [nucl-ex]]. [2](#), [9](#)
34. H. Gao and M. Vanderhaeghen, Rev. Mod. Phys. **94**, no.1, 015002 (2022) [arXiv:2105.00571 [hep-ph]]. [2](#)
35. W. Xiong and C. Peng, Universe **9**, no.4, 182 (2023) [arXiv:2302.13818 [nucl-ex]]. [2](#)
36. I. Akushevich, H. Gao, A. Ilyichev and M. Meziane, Eur. Phys. J. A **51**, no.1, 1 (2015). [2](#), [4](#), [5](#), [6](#), [7](#), [8](#), [11](#)
37. A. B. Arbuzov and T. V. Kopylova, Eur. Phys. J. C **75**, no.12, 603 (2015). [2](#), [7](#), [10](#), [11](#)
38. I. Sick and D. Trautmann, Nucl. Phys. A **637**, 559 (1998). [2](#)
39. I. Sick, Prog. Part. Nucl. Phys. **47**, 245-318 (2001). [2](#)
40. E. Tiesinga, P. J. Mohr, D. B. Newell and B. N. Taylor, Rev. Mod. Phys. **93**, no.2, 025010 (2021). [2](#)
41. R. Pohl *et al.*, Science **353**, 669 (2016). [2](#)
42. R. Pohl *et al.*, Metrologia **54**, L1 (2017) [arXiv:1607.03165 [physics.atom-ph]]. [2](#)
43. C. G. Parthey, A. Matveev, J. Alnis, R. Pohl, T. Udem, U. D. Jentschura, N. Kolachevsky and T. W. Hänsch Phys. Rev. Lett. **104**, 233001 (2010). [2](#)
44. PRad Collaboration, Precision Deuteron Charge Radius Measurement with Elastic Electron-Deuteron Scattering, [https://www.jlab.org/exp\\_prog/proposals/17/PR12-17-009.pdf](https://www.jlab.org/exp_prog/proposals/17/PR12-17-009.pdf) [2](#), [12](#)
45. I. Akushevich and N. Shumeiko, J. Phys. G **20**, 513-530 (1994). [2](#), [4](#), [6](#), [7](#), [11](#)
46. I. Akushevich, A. Ilyichev and N. Shumeiko, Radiative effects in scattering of polarized leptons by polarized nucleons and light nuclei, [arXiv:hep-ph/0106180 [hep-ph]]. [2](#), [7](#), [11](#)
47. A. Afanasev, I. Akushevich and N. Merenkov, Phys. Rev. D **64**, 113009 (2001) [arXiv:hep-ph/0102086 [hep-ph]]. [2](#), [11](#)
48. I. Akushevich and A. Ilyichev, Phys. Rev. D **100**, no.3, 033005 (2019) [arXiv:1905.09232 [hep-ph]]. [2](#), [4](#), [6](#), [11](#)
49. A. Ilyichev and V. Zykunov, Phys. Rev. D **72**, 033018 (2005) [arXiv:hep-ph/0504191 [hep-ph]]. [2](#), [11](#)
50. I. Akushevich, A. Ilyichev and M. Osipenko, Phys. Lett. B **672**, 35-44 (2009) [arXiv:0711.4789 [hep-ph]]. [2](#), [11](#)
51. V. A. Zykunov, Phys. At. Nucl. **84**, no.5, 739-749 (2021). [2](#)

52. A. Afanasev and A. Ilyichev, *Eur. Phys. J. A* **57**, no.9, 280 (2021) [arXiv:2106.11103 [hep-ph]]. [2](#), [4](#), [5](#), [6](#), [7](#), [8](#), [9](#), [11](#), [14](#)
53. A. Afanasev and A. Ilyichev, *Eur. Phys. J. A* **58**, no.8, 156 (2022) [arXiv:2202.11497 [hep-ph]]. [2](#), [11](#)
54. L. C. Maximon and J. A. Tjon, *Phys. Rev. C* **62**, 054320 (2000) [arXiv:nucl-th/0002058 [nucl-th]]. [2](#)
55. A. V. Gramolin, V. S. Fadin, A. L. Feldman, R. E. Gerasimov, D. M. Nikolenko, I. A. Rachek and D. K. Toporkov, *J. Phys. G* **41**, no.11, 115001 (2014) [arXiv:1401.2959 [nucl-ex]]. [2](#)
56. R. D. Bucoveanu and H. Spiesberger, *Eur. Phys. J. A* **55**, no.4, 57 (2019) [arXiv:1811.04970 [hep-ph]]. [2](#), [12](#)
57. R. D. Bucoveanu and H. Spiesberger, *PoS SPIN2018*, 115 (2019) [arXiv:1903.12229 [hep-ph]]. [2](#)
58. V. S. Fadin and R. E. Gerasimov, *Phys. Lett. B* **795**, 172-176 (2019) [arXiv:1812.10710 [nucl-th]]. [2](#)
59. P. Banerjee, T. Engel, A. Signer and Y. Ulrich, *SciPost Phys.* **9**, 027 (2020) [arXiv:2007.01654 [hep-ph]]. [2](#), [12](#)
60. N. Kaiser, Y. H. Lin and U. G. Meißner, *Phys. Rev. D* **105**, no.7, 076006 (2022) [arXiv:2202.04409 [hep-ph]]. [2](#)
61. B. Schmookler, A. Pierre-Louis, A. Deshpande, D. Higinbotham, E. Long and A. J. R. Puckett, High  $Q^2$  electron-proton elastic scattering at the future Electron-Ion Collider, [arXiv:2207.04378 [nucl-ex]]. [2](#)
62. N. M. Shumeiko and J. G. Suarez, *J. Phys. G* **26**, 113-127 (2000) [arXiv:hep-ph/9912228 [hep-ph]]. [2](#)
63. N. Kaiser, *J. Phys. G* **37**, 115005 (2010) [2](#)
64. C. S. Epstein and R. G. Milner, *Phys. Rev. D* **94**, no.3, 033004 (2016) [arXiv:1602.07609 [nucl-ex]]. [2](#)
65. A. G. Alekseyevs, S. G. Barkanova, V. A. Zykunov and E. A. Kuraev, *Phys. of Atom. Nucl.* **76**, 888 (2013). [2](#), [12](#)
66. A. G. Alekseyevs, S. G. Barkanova, Y. M. Bystritskiy and V. A. Zykunov, *Phys. Part. Nucl.* **51**, no.4, 645-650 (2020) [arXiv:2010.12579 [hep-ph]]. [2](#)
67. P. Banerjee, T. Engel, N. Schalch, A. Signer and Y. Ulrich, *Phys. Lett. B* **820**, 136547 (2021) [arXiv:2106.07469 [hep-ph]]. [2](#)
68. P. Banerjee, T. Engel, N. Schalch, A. Signer and Y. Ulrich, *Phys. Rev. D* **105**, no.3, 3 (2022) [arXiv:2107.12311 [hep-ph]]. [2](#)
69. S. G. Bondarenko, L. V. Kalinovskaya, L. A. Romyantsev and V. L. Yermolchik, One-loop electroweak radiative corrections to polarized Møller scattering, [arXiv:2203.10538 [hep-ph]]. [2](#)
70. D. Y. Bardin and N. M. Shumeiko, *Nucl. Phys. B* **127**, 242-258 (1977). [2](#), [5](#)
71. N. M. Shumeiko, *Sov. J. Nucl. Phys.* **29**, 807 (1979). [2](#), [5](#), [7](#)
72. G. I. Gakh, M. I. Konchatnij, N. P. Merenkov and E. Tomasi-Gustafsson, *Phys. Rev. C* **98**, no.4, 045212 (2018) [arXiv:1804.01399 [hep-ph]]. [2](#), [14](#)
73. J. Zhou, V. Khachatryan, H. Gao, D. W. Higinbotham, A. Parker, X. Bai, D. Dutta, A. Gasparian, K. Gnanvo and M. Khandaker, *et al. Phys. Rev. C* **103**, no.2, 024002 (2021) [arXiv:2010.09003 [nucl-ex]]. [2](#), [13](#)
74. X. Yan, D. W. Higinbotham, D. Dutta, H. Gao, A. Gasparian, M. A. Khandaker, N. Liyanage, E. Pasyuk, C. Peng and W. Xiong, *Phys. Rev. C* **98**, no.2, 025204 (2018) [arXiv:1803.01629 [nucl-ex]]. [3](#)
75. Z. F. Cui, D. Binosi, C. D. Roberts and S. M. Schmidt, *Chin. Phys. C* **46**, no.12, 122001 (2022) [arXiv:2204.05418 [hep-ph]]. [3](#)
76. Z. F. Cui, D. Binosi, C. D. Roberts and S. M. Schmidt, *Phys. Rev. Lett.* **127**, no.9, 092001 (2021) [arXiv:2102.01180 [hep-ph]]. [3](#)
77. A. A. Filin, V. Baru, E. Epelbaum, H. Krebs, D. Möller and P. Reinert, *Phys. Rev. Lett.* **124**, no.8, 082501 (2020) [arXiv:1911.04877 [nucl-th]]. [3](#)
78. A. A. Filin, D. Möller, V. Baru, E. Epelbaum, H. Krebs and P. Reinert, *Phys. Rev. C* **103**, no.2, 024313 (2021) [arXiv:2009.08911 [nucl-th]]. [3](#)
79. C. W. Wong, *Int. J. Mod. Phys. E* **3**, 821 (1994). [3](#)
80. R. G. Arnold, C. E. Carlson and F. Gross, *Phys. Rev. C* **23**, 363 (1981) [3](#), [4](#)
81. T. W. Donnelly and A. S. Raskin, *Annals Phys.* **169**, 247-351 (1986). [4](#)
82. F. Coester and A. Ostebee, *Phys. Rev. C* **11**, 1836 (1975) [4](#)
83. D. Abbott *et al.* [JLab t20 Collaboration], *Eur. Phys. J. A* **7**, 421 (2000) [nucl-ex/0002003], <http://irfu.cea.fr/dphn/T20/Parametrisations/> [4](#), [13](#), [14](#)
84. A. P. Kobushkin and A. I. Syantomov, *Phys. Atom. Nucl.* **58**, 1477 (1995) [*Yad. Fiz.* **58N9**, 1565 (1995)]. [4](#), [13](#)
85. J. C. Bernauer, Measurement of the elastic electron-proton cross section and separation of the electric and magnetic form factor in the  $Q^2$  range from 0.004 to 1 (GeV/c)<sup>2</sup>, Thesis: PhD Mainz U., *Inst. Kernphys.* (2010). [4](#)
86. W. Greiner and J. Reinhardt, *Quantum Electrodynamics*, ISBN: 978-3-540-87561-1, Springer (2009). [4](#)
87. W. Xiong, A High Precision Measurement of the Proton Charge Radius at JLab, Thesis: PhD Duke U. (2020). [4](#), [8](#), [12](#)
88. D. Byer, V. Khachatryan, H. Gao, I. Akushevich, A. Ilyichev, C. Peng, A. Prokudin, S. Srednyak and Z. Zhao, *Comput. Phys. Commun.* **287**, 108702 (2023) [arXiv:2210.03785 [hep-ph]]. [4](#), [7](#)
89. L. W. Mo and Y. S. Tsai, *Rev. Mod. Phys.* **41**, 205-235 (1969). [5](#)
90. Y. S. Tsai, Radiative corrections to electron scattering, SLAC-PUB-0848. [5](#)
91. F. Jegerlehner, "Electroweak effective couplings for future precision experiments," *Nuovo Cim. C* **034S1**, 31-40 (2011) [arXiv:1107.4683 [hep-ph]], <http://www-com.physik.hu-berlin.de/~fjeger/software.html> [7](#)
92. J. Zhou, DRad e-d event generator, (2023), <https://github.com/TooLate0800/edevgen> [8](#), [9](#)
93. C. Peng, PRadAnalyzer, (2017), <https://github.com/JeffersonLab/PRadAnalyzer> [8](#), [10](#)
94. RADIATIVE CORRECTION HELPDESK, MASSRAD, (2022), <https://www.hep.by/RC> [8](#)
95. O. Tomalak, *Few Body Syst.* **59**, no.5, 87 (2018) [arXiv:1806.01627 [hep-ph]]. [12](#)
96. O. Tomalak and M. Vanderhaeghen, *Phys. Rev. D* **93**, no.1, 013023 (2016) [arXiv:1508.03759 [hep-ph]]. [12](#)
97. O. Tomalak and M. Vanderhaeghen, *Eur. Phys. J. A* **51**, no.2, 24 (2015) [arXiv:1408.5330 [hep-ph]]. [12](#)
98. Y. H. Lin, H. W. Hammer and U. G. Meißner, *Phys. Lett. B* **827**, 136981 (2022) [arXiv:2111.09619 [hep-ph]]. [12](#)
99. J. F. Gunion and L. Stodolsky, *Phys. Rev. Lett.* **30**, 345 (1973). [12](#)
100. V. Franco, *Phys. Rev. D* **8**, 826-828 (1973). [12](#)
101. Y. B. Dong and D. Y. Chen, *Phys. Lett. B* **675**, 426-432 (2009) [arXiv:0905.1406 [nucl-th]]. [12](#)
102. D. Richards and C. Weiss, Private communication. [12](#)
103. A. Parker and D. W. Higinbotham, Deuteron Form Factor Parameterization, (2020), <https://doi.org/10.5281/zenodo.4074280>, [https://github.com/shrewberry/Form\\_Factor\\_SULI2020\\_Parameterization](https://github.com/shrewberry/Form_Factor_SULI2020_Parameterization) [13](#)
104. I. Sick, *Nucl. Phys. A* **218**, 509-541 (1974). [14](#)
105. J. Zhou, The Sum-of-Gaussian parameterizations fitted with the available deuteron form factor data, (2020), [https://github.com/TooLate0800/Deuteron\\_radius\\_fitting/tree/master/SOG\\_fitting](https://github.com/TooLate0800/Deuteron_radius_fitting/tree/master/SOG_fitting) [14](#)